Chapter 18
Uncovering Radiation Chemistry in the Solid State Through Periodic Density-Functional Calculations: Confrontation with Experimental Results and Beyond

Ewald Pauwels

Abstract Three questions are crucial to unravel the radiation chemistry of any solid-state molecular system: what is the structure of the radicals formed, how are they formed and why? Molecular modeling methods based on Density Functional Theory—in confrontation with experimental Electron Paramagnetic Resonance (EPR) results—can help in finding an answer to all three questions. In this contribution, one view on how to perform such computational research is presented, with emphasis on the application of a periodic approach to biomolecules such as amino acids and carbohydrates. General strategies are outlined and common pitfalls are indicated. Topics include: effect of level of theory, model space and temperature on calculated EPR properties, formation mechanisms of radiation-induced radicals, and reaction path simulations for radiochemical transformations. In three case studies, these principles are applied to several radiation-induced radicals of sucrose.

18.1 Introduction

The chemical processes and conformational changes to the radicals that are generated in condensed-phase systems as a consequence of radiation damage have been of interest for many years [1]. The advent of EPR spectroscopy and derived techniques has sparked a way to elucidate these processes and analyze which radicals are generated *in situ* by radiation, owing greatly to their longevity in this phase.

Ever since the emergence of EPR as the leading technique to obtain insight into the radiation-induced processes, first-principles calculations—in some form or other—have been used to facilitate the analysis and interpretation of the spectroscopic properties. Ranging from the "simple" Heller-McConnell relations

E. Pauwels (✉)
UGent HPC, Ghent University, Krijgslaan 281 S9, B-9000 Gent, Belgium
e-mail: ewald.pauwels@ugent.be

Center for Molecular Modeling, Ghent University,
Technologiepark 903, B-9052 Zwijnaarde, Belgium

A. Lund, M. Shiotani (eds.), *Applications of EPR in Radiation Research,*
DOI 10.1007/978-3-319-09216-4_18

[2, 3], over semi-empirical INDO calculations (e.g. [4]) to current-day density functional theory (DFT) calculations, an interesting historical perspective on the use of calculations has been presented by Neese and Munzarova in the seminal book by Kaupp, Bühl and Malkin [5].

Disregarding the hardships in performing EPR measurements for a moment, deriving structural and mechanistic information from the resulting spectroscopic properties is usually hard and open to ambiguity, certainly for condensed-phase molecular systems. First-principles calculations, and DFT in particular, have provided the experimentalist with a formidable tool to reach new insight into the radiation chemistry. Not surprisingly, ever since 1995, joint computational-experimental research in this respect has steadily grown in popularity.

In this contribution, I present my point of view on how molecular modeling methods can be applied to elucidate radiation chemistry in condensed-phase systems. I will draw heavily on experiences throughout 13-odd years of computational research, often in collaboration with several experimental EPR groups, focusing on two types of solid-state biomolecules: amino acids and carbohydrates. Both systems are abundantly present in the natural world and are vital to the existence of life in all its forms. They can therefore be considered as model systems to examine radiation chemistry and the principles that govern it on a molecular level.

Three questions are key to unravel the radiation chemistry for condensed-phase molecular systems:

1. *WHAT?*—What is the structural identity of the radiation-induced radicals that are generated in the (solid-state) matrix?
2. *HOW?*—Through which processes are these radicals formed and which conformational changes take place to transform one radical structure into another?
3. *WHY?*—Why do we see the radicals that we see? Radiation clearly favors the production of specific radicals. What is the origin of this specificity? Or rather, why are only specific radicals formed by radiation?

It goes without saying that solution of question 2 or 3 requires a solution of all preceding questions. Below, I will outline how molecular modeling methods, in confrontation with experimental data, can contribute to solving these questions. For reasons that will become clear, I will rely solely on periodic DFT calculations (using the CP2K software package [6, 7]) since this methodology is most apt to treat the solid state.

Several radiation-induced radicals in (crystalline) sucrose will serve to illustrate the discussion via three case studies. The motivations for studying these radicals have already been elaborately discussed in Chap. 6 of this book. Recent developments on the radiation chemistry of sucrose were brought about by De Cooman et al., often relying on a combined experimental-computational approach [8–11]. In this work, new computational research will add to that body of work, although these new calculations mainly serve a didactic purpose.

Whenever possible, proper reference to key studies was made, but literature was not scanned exhaustively. I apologize if, in this process, an important study was overlooked.

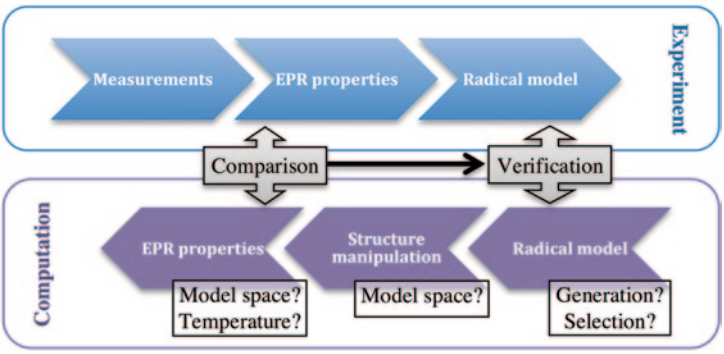

Fig. 18.1 General strategy to identify the structure of radiation-induced radicals by confronting *experiment* and *computation*

18.2 Identifying Radiation-Induced Radicals—*WHAT?*

18.2.1 General Strategy

An essential prerequisite to solving the *WHAT?* question is that the radiation-induced radicals in the molecular system under question have already been examined with the aid of EPR spectroscopy. Without it, confrontation between computation and experiment is obviously not possible, and, despite 50-odd years of research, still not enough is known about radiation chemistry to start making educated guesses. When hyperfine coupling tensors and/or g-tensor (and possibly even zero-field splitting tensor) for a specific radical are available, confrontation with molecular modeling computations is possible. The general strategy to identify the structure of radiation-induced radicals in this way is illustrated in Fig. 18.1.

In the experimental setup, structural information regarding a radiation-induced radical species is deduced by thorough analysis of spectroscopic properties, obtained through EPR, ENDOR and/or EIE studies. For instance, the principal directions of the hyperfine coupling tensors can be compared to interatomic directions observed in the pristine crystal structure, or conformational information can be obtained from the Heller-McConnell relations [2, 3]. Both have been applied frequently to examine the radiation-induced radicals in carbohydrates, amino acids or other biomolecules (e.g. [12–15]).

In molecular modeling, this procedure is instead reversed and one starts out by proposing one or more radical models. Subsequently, the initial structures for these selected radical models are subject to some form of structure manipulation. Usually, a stable radical conformation—a global (or local) energetic minimum in terms of all possible degrees of freedom—is sought via an energy minimization algorithm. Alternatively, molecular dynamics simulations can be used here to explore the conformational space of the radical model. Next, the EPR properties are calculated for the optimal radical conformation. DFT is quite successful in determining such properties, owing largely to advances in the theoretical framework. See the reference

work by Kaupp, Bühl and Malkin [5] for an in-depth treatment on this subject. For the periodic implementations in the CP2K code, consult references [16, 17].

By now comparing measured and calculated EPR properties with each other, the validity of the radical model can be verified: if the spectroscopic properties match within reasonable extent, the proposed radical model in the DFT calculations is likely correct. If not, the experimentally observed radical species probably has a different structure.

A perfect agreement between theory and experiment with respect to the EPR properties is almost never obtained. To assess the agreement, one has to look at the characters of the hyperfine coupling tensors involved (α-type, β-type), the size of the isotropic and anisotropic couplings (or g-tensor components), the agreement between corresponding eigenvectors. Especially the eigenvector directions (for both g- and hyperfine tensors) turn out to be good gauges for the validity of a radical model [18], in contrast with the size of the isotropic coupling, which can vary considerably with the density functional and the extent of the basis set chosen [19].

18.2.2 Case Study 1: Sucrose Radical R2

In the body of work produced by De Cooman et al. on the radiation chemistry of sucrose, several radicals have been unequivocally identified using a combination of EPR experiments and a computational approach (see Chap. 6 and Refs. [8–11]). One of these is R2, a radical likely produced via the oxidative branch in the radiation chemistry of sucrose. This species was observed after in situ X irradiation at 10 K and EPR measurements at the same temperature [9]. R2 is one of four dominant species present in the crystalline matrix at this low temperature, indicating that it is a primary radiation-induced radical. It is characterized by only one hyperfine coupling tensor (see Table 18.1) for a non-exchangeable proton, as determined from EPR measurements on deuterated crystals. Below, the procedure leading up to a positive structural identification for this radical is reprised, consistent with the methodology in Fig. 18.1.

Given that R2 is a primary radiation-induced radical, no major changes to the carbohydrate structure can be expected as a result of the radiative action: simple hydrogen abstractions may be considered as a first possibility. The measured hyperfine coupling tensor is indicative of a non-exchangeable β-type proton, which is therefore directly bound to a carbon adjacent the site of the unpaired electron. However, not all carbons C1 to C6 and C1′ to C6′ (see Fig. 18.2 for the atom numbering scheme in sucrose) are possible locations for net hydrogen abstraction and the site of the unpaired electron: one and only one hyperfine coupling tensor was recorded, excluding the possibility that α-type or other β-type protons would interact with the unpaired electron. In principle, this excludes sites C2, C3, C4, C5, C6 in the glucopyranose unit of sucrose, and C1′, C4′, C5′, C6′ in the fructofuranose unit, leaving as only remaining possibilities hydrogen abstraction from C1 or from C3′. The molecular structures of these models—referred to as M(C1) and M(C3′)—are shown in Fig. 18.2. In a very simplistic approach, only these radical models would be considered in the computational cycle.

Table 18.1 Overview of EPR properties for radical species R2 (taken over from Ref. [9]) and for models M(C1) and M(C3′), as obtained from periodic DFT calculations. Isotropic (A_{iso}) and anisotropic hyperfine couplings (A_{aniso}) are in MHz. Principal directions are given with respect to the orthogonal <a*bc> reference frame. The last column indicates the angle (in degrees) between corresponding experimental and calculated eigenvector directions. Note that calculated tensors slightly differ from those reported in [9] since a larger periodic cell was considered in that study: the unit cell duplicated along the crystallographic *c* axis

Atom/ Coupling	A_{iso}	A_{aniso}	Principal directions			Angle
Experiment: R2						
HF1	29.88	−5.93	0.759	−0.001	−0.651	
		−4.80	0.272	0.909	0.316	
		10.73	0.591	−0.417	0.690	
Computation: M(C1)						
H(C2)	30.43	−5.86	0.791	0.058	−0.609	4.5
		−4.54	0.230	0.894	0.384	4.6
		10.40	0.567	−0.444	0.694	2.1
Computation: M(C3′)						
H(C1′)	13.13	−2.17	0.441	0.898	−0.009	70.2
		−0.79	−0.766	0.381	0.517	72.4
		2.96	0.468	−0.221	0.856	16.4
H(C4′)	96.45	−6.16	0.893	0.348	−0.284	30.3
		−0.95	−0.266	0.920	0.289	31.3
		7.12	0.362	−0.182	0.914	22.9
H(O2′)	120.63	−8.40	0.032	−0.040	−0.999	47.6
		−5.97	0.998	0.061	0.030	70.3
		14.37	0.060	−0.997	0.042	61.3

However, the hyperfine coupling of a β-type proton is very sensitive to its orientation with respect to the site of the unpaired electron (which is immediately clear from the Heller-McConnell relation—see Chap. 6 or Ref. [2]). It is not inconceivable that its orientation in the radical is such that the corresponding hyperfine coupling is weak in strength and that it remained undetectable in the EPR measurements. Hence, the absence of a β-type coupling in the experiment does not necessarily mean that there are no protons in the radical in a β-position with respect to the unpaired electron. Hydrogen abstractions from C2, C3, C4, C5, C4′ or C5′ should therefore not be rejected *a priori*. Only models M(C6), M(C1′) and M(C6′) can be safely disregarded as they would yield a clear α-type hyperfine coupling (which hardly goes undetected in EPR or ENDOR spectra). This brings the total of radical models to be investigated with DFT to eight: M(C1), M(C2), M(C3), M(C4), M(C5), M(C3′), M(C4′), M(C5′).

In the original paper by De Cooman et al. [9] a further reduction of tentative radical models was made. A point-dipole approximation was used and the direction of the eigenvector associated with the most positive principal hyperfine coupling value was compared with various interatomic directions in the pristine crystal lattice of sucrose. In this way, the list of potential candidates was reduced from eight to three.

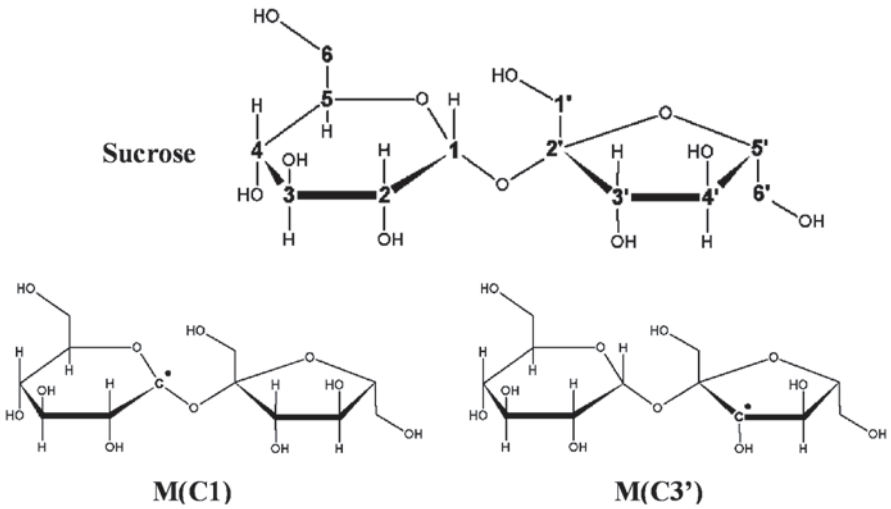

Fig. 18.2 *Top*: molecular structure of *sucrose* and atom numbering scheme. *Bottom*: molecular structure of radical models *M(C1)* and *M(C3')*

The validity of the point-dipole approximation, however, hinges on the structural and conformational similarity of the radical and the crystal structure. If the radical assumes a dramatically different conformation, the correct radical model might be falsely disregarded. In this work, all eight potential candidates are considered, albeit with more emphasis on models M(C1) and M(C3′) for illustrative purposes.

For all selected models, initial geometries are created, illustrated in Fig. 18.3 for M(C1) and M(C3′). One of the molecules in the crystallographic unit cell of sucrose is adapted in accordance with the chemical structure of the radical model. In this case, the hydrogen bound to C1 or C3′ is simply removed from the periodic cell altogether, yielding the initial geometries. Subsequently, these are subject to energy minimization using a limited memory version of the Broyden–Fletcher–Goldfarb–Shanno (BFGS) algorithm [21]. The BLYP density functional [22, 23] is used in conjunction with the Gaussian and plane waves (GPW) dual basis set method [24] using a TZVP triple-ζ Gaussian basis set [25] and plane waves (400 Ry density cut-off) with GTH pseudopotentials [26, 27]. The optimized geometries are shown on the right hand side of Fig. 18.3. For both radical models, the final optimized conformation is very similar to that of the initial geometry. Similar energy minimizations are also performed for the other radical models.

The EPR properties can now be calculated for the optimized geometries of all eight radical models, relying on recent implementations [16, 17] in CP2K [6, 7] and the all-electron Gaussian and augmented plane wave (GAPW) method [28]. The density cut-off of the auxiliary plane wave basis is set to 200 Ry and the all-electron TZVP basis [29] is used. Note that not necessarily the same basis set, density

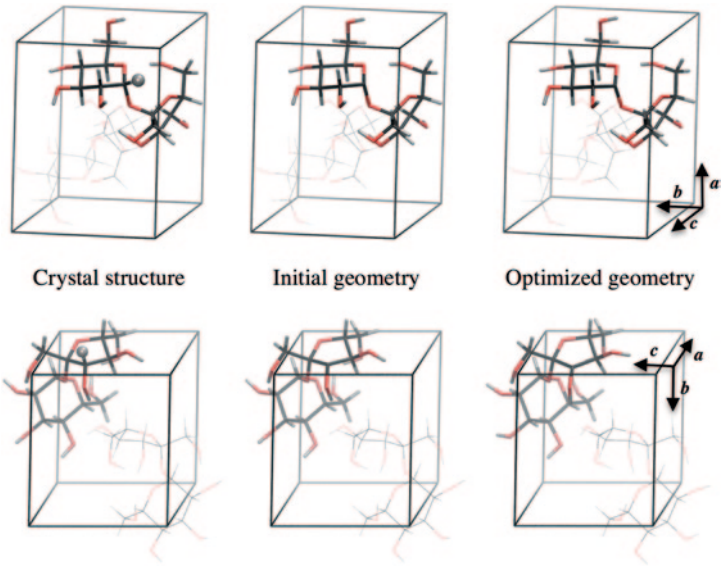

Fig. 18.3 From *crystal structure* to *optimized geometry* for radical models M(C1) (*top*) and M(C3′) (*bottom*). In one molecule in the unit cell (shown as *licorice*), a single proton is removed (shown as *sphere*) to generate the initial geometry. Energy minimization of that structure yields the *optimized geometry*. 3D-renders produced with the aid of VMD [20]

functional or plane wave approach need to be followed in the EPR calculation and the structure manipulation steps. In fact, the dual methodology outlined above has proven quite successful in various other studies [30–33].

The calculated EPR properties are listed in Table 18.1 for models M(C1) and M(C3′), and in Table 18.2 for the other six radical models. From a qualitative point of view, only one radical model meets the one-hyperfine-tensor-only criterion: M(C1). All the others have at least one other significant proton hyperfine coupling interaction. Also, not many of the calculated tensors display the almost prototypical β-type character of the measured HF1 interaction in radical R2 (see Table 18.1): H(C2) in M(C1), H(C1) in M(C2), H(C6)a/b in M(C5) and H(C6′)a/b in model M(C5′). Of these, only H(C2) matches quantitatively with the experimental HF1 coupling, both for the isotropic and anisotropic parts. Furthermore, the principal directions for this calculated hyperfine tensor are very similar to those of the experiment. The deviation (expressed in degrees) between corresponding directions is below 5° at all times, which is an extremely good agreement. None of the principal directions in the other calculated hyperfine tensors come even close.

Reviewing the agreement between calculated and measured hyperfine tensors, there is very little doubt that the structure of radical R2 observed experimentally corresponds to that of radical model M(C1). Our new simulations therefore concur with the results of De Cooman et al. [9].

Table 18.2 Overview of calculated EPR properties for various hydrogen abstraction radical models of sucrose. Isotropic (A_{iso}) and anisotropic hyperfine couplings (A_{aniso}) are in MHz. The angle (in degrees) indicates the agreement in direction between the calculated eigenvectors and those of the experimental HF1 tensor (see Table 18.1)

Atom	A_{iso}	A_{aniso}	Angle	Atom	A_{iso}	A_{aniso}	Angle
M(C2)				*M(C3)*			
H(C1)	26.61	−5.72	32.7	H(C2)	96.60	−4.61	52.6
		−3.86	66.7			−2.35	56.5
		9.58	56.8			6.95	27.6
H(C3)	98.33	−5.15	23.8	H(C4)	84.43	−4.85	75.2
		−0.97	28.6			−1.68	43.7
		6.12	24.3			6.53	76.2
H(O2)	3.48	−10.60		H(O3)	−7.44	−11.55	
		−9.10				−8.30	
		19.70				19.85	
M(C4)				*M(C5)*			
H(C3)	88.79	−5.57	81.8	H(C4)	94.55	−5.29	43.3
		−0.77	63.4			−1.24	46.4
		6.34	79.0			6.54	18.0
H(C5)	88.67	−4.33	29.2	H(C6)a	2.84	−6.00	63.8
		−2.65	28.9			−3.54	75.0
		6.98	17.8			9.54	63.6
H(O4)	−5.11	−11.27		H(C6)b	15.61	−6.01	75.1
		−8.35				−3.49	59.0
		19.62				9.50	60.1
M(C5′)				H(O6)	−4.31	−7.59	
H(C4′)	69.20	−4.92	37.0			0.45	
		−2.31	39.6			7.14	
		7.24	30.0	*M(C4′)*			
H(C6′)a	5.40	−5.75	64.8	H(C3′)	81.90	−5.14	71.5
		−3.45	22.1			−1.58	7.9
		9.20	60.2			6.72	71.6
H(C6′)b	9.31	−6.39	72.8	H(C5′)	80.11	−4.52	26.3
		−3.43	46.0			−2.62	39.9
		9.83	64.7			7.14	45.8
H(O6′)	−5.36	−8.80		H(O4′)	−4.00	−12.21	
		0.70				−9.16	
		8.10				21.38	

18.2.3 Radical Model Generation and Selection

As case study 1 points out, selecting a radical model to initiate the DFT calculation cycle is not trivial. Nor is generating an initial structure for the selected model. Usually, an initial structure for the radical is generated by introducing alterations to the crystallographic structure of the molecule under study, e.g. by removing a hydrogen atom. These alterations should reflect the action of the radiation damage, but proposing and executing these alterations is very hands-on. One can usually draw on prevailing radiation chemistry theories [34] for inspiration, but human

interaction is always required. Also, often a large amount of candidate structures must be examined before a radical model is found with calculated EPR properties that successfully match with experiment. The case of R2 is 'lucky' in that respect, since only eight models were required. But in some cases, even a cornucopia of candidate models is not enough to home in on the true identity of a radiation-induced radical: the structure of the room-temperature radical in β-D-fructose is still a mystery [35] even though over 60 different models have been examined.

The level of 'realism' that is introduced by the structural alterations in the computational approach is also important. Removing a hydrogen atom altogether from the crystal structure corresponds to the situation where radiation has knocked off the hydrogen, which has then—somehow—diffused throughout the crystal, away from the radical site. This simple approach has worked wonderfully well in various carbohydrates, amino acids and other biomolecules (e.g. [8–11, 13, 18, 35–43]). Alternatively, the abstracted hydrogen might stick around in the vicinity of the radical, influencing its molecular environment and also its EPR properties. This latter situation is even more likely to apply when larger molecular fragments are involved, such as abstracted hydroxyl or even larger groups. In these cases, it might be necessary to include those abstracted fragments in the molecular model in order to get a good agreement between measured and calculated EPR properties. Knowing exactly in what way the radiation damage proceeds, which processes and conformational changes are involved (i.e. solving the *HOW?* question) then becomes a prerequisite for identification. In alanine, such an examination was required to identify the structure of the main room temperature stable radical [30].

As problematic cases (such as the elusive room-temperature radical in β-D-fructose [35]) point out, coming up with new radical models to input at the computational side of the identification process can be a limiting factor. This is due to, what I often call, the *human Monte Carlo algorithm* that is used to furnish new radical models: a human needs to come up with a bright new idea of what structure a particular radical could have. Inspiration from established radiation chemistry [34] or human imagination only go so far, and so this poses a big challenge to joint computational-experimental EPR studies into radiation chemistry.

One way to surpass this bottleneck is by automating the way in which possible radical models are generated: implementing a *non-human Monte Carlo algorithm*. To the best of my knowledge, no substantial research has been conducted in this field. Perhaps the approach by Tachikawa et al. [44, 45] comes close: direct ab-initio molecular dynamics is used to examine the structural and conformational events immediately following a drastic change in the potential energy surface (e.g. going from a neutral to an ionized and paramagnetic state). Whether a similar approach could be useful as a semi-automated *generator* for potential radical models in carbohydrates or other biomolecules requires further computational research [46].

18.2.4 Model Space

For condensed phase systems, the most important computational parameter throughout the computational cycle is the *model space*: the extent with which the molecular

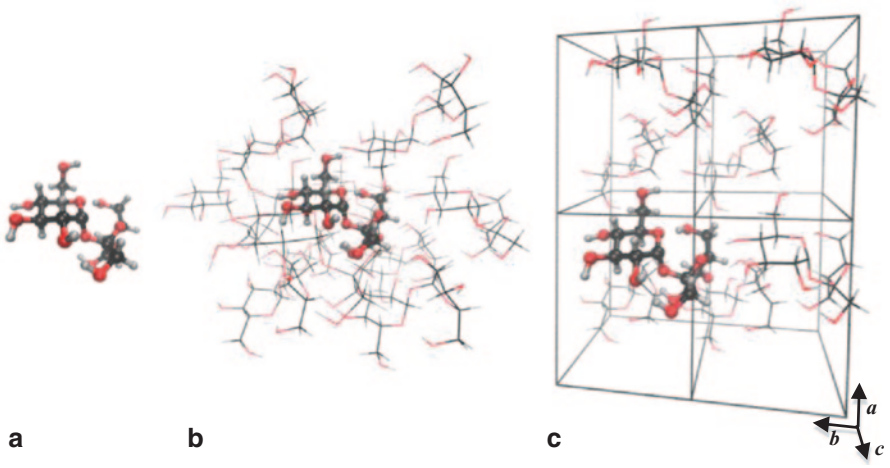

Fig. 18.4 Illustration of the three model space approaches applied to the R2 radical structure of sucrose: single molecule (**a**), cluster (**b**) and periodic approach (**c**). The radical is represented by "ball-and-stick", its molecular environment in the model space approach by *lines*. Note that, in the cluster approach, considerably more surrounding molecules must be taken up in the model as compared to the periodic approach. 3D-renders produced with the aid of VMD [20]

environment of a radiation-induced radical is taken up in the DFT calculation. This aspect is of importance in the 'structure manipulation' as well as the 'EPR calculation' steps. Three types of model space approaches can be distinguished. Illustrative examples for sucrose are shown in Fig. 18.4.

Single Molecule Approach The simplest approximation is to completely neglect the molecular environment. In this approach, the optimal conformation of the radical is determined in a vacuum. The obvious benefit is the simplicity of the model and concomitant speed of the calculation. The downside is that all-important intermolecular interactions in the solid state are not at all incorporated in the computational model. Nevertheless, this approximation can be used with success and remains quite popular.

Cluster Model Approach One rung up is to include the medium in a so-called cluster model: a small part of the crystal lattice is explicitly modeled, by placing discrete molecules around the target radical. Though this offers an immediate, easy way of including some intermolecular interactions (e.g. all hydrogen bonds in the crystal), this model space can be totally unreliable [40]. For the main radiation-induced radical in solid-state α-glycine, for example, the selection of the number and position of the pristine molecules surrounding the radical proved to determine the results heavily, but in a seemingly unphysical way: larger clusters offered a *worse* description of the solid state than smaller ones. In addition to their unreliability related to the biased or arbitrary selection of molecules to include, cluster models tend to impose a considerable computational burden, especially in comparison with a periodic approach. Furthermore, constraints have to be imposed to the molecules at the outskirts of the cluster. These molecules are in contact with the

vacuum and need to be held in place in one way or another to prevent the entire cluster from distorting, possibly altering the bulk-like interactions at the center of the cluster. This can give rise to boundary problems [18].

Periodic Approach This approach offers the most natural and cost-effective way of describing the solid-state environment. The model space consists of the actual crystallographic unit cell, which is subject to periodic boundary conditions, in which a certain amount of radical defects has been introduced. In the sucrose example outlined below, this is achieved by altering one of the two molecules in the unit cell. Depending on how densely the molecules are packed together in the crystal, it might be necessary to double the original unit cell in one or more crystal directions, to ensure that the radical defects are sufficiently separated from each other under periodic boundary conditions.

The model space treatment in any computational approach has a severe impact on the results that are obtained. In an energy minimization ('structure manipulation' step), neglect of the medium can lead to erroneous conformations. Sometimes this is blatantly apparent: zwitterionic amino acids *cannot* be properly described in a single molecule approach and undergo intramolecular proton transfer [36]. But in other cases the effect can be more subtle, leading to erroneous identification of radical structures (e.g. in fructose [47]) or unjustified rejection of a candidate radical structure. An extensive analysis of the effect of the model space on radical conformation (and concomitantly the EPR properties) has been conducted on the main glycine radical [18].

The model space is also important in the calculation of the EPR properties, irrespective of its effect on the conformation of the radical. As shown by Declerck et al. on glucose and fructose radicals [37], the model space alone can have a direct influence on the hyperfine coupling tensors: calculated principal directions can easily deviate by 30°, and the isotropic coupling size can vary by as much as 20 MHz. But even more fundamentally, an appropriate model space approximation needs to be in place to properly compare the calculated principal directions of g- and hyperfine tensors with their experimental counterparts.

In experiment, principal directions are specified as direction cosines with respect to the crystal axes (or an orthogonal projection of them). Calculated principal directions must therefore also be specified with respect to the same reference frame for proper comparison. In a periodic or cluster approach, some part of the undamaged crystal is comprised in the model space and consequently the orientation of the crystal axes is always known. Thus, whatever conformational changes the radical undergoes during the 'structure manipulation' step, the absolute orientation of the resulting structure(s) with respect to the crystal axes can at all times be traced. In a single molecule approach, on the other hand, no such information is retained during the calculation, and analysis of calculated principal directions becomes more cumbersome. One way to get by this problem is to assume that the global orientation of the radical does not change dramatically with respect to the pristine crystal structure (in the Gaussian software [48], this is most easily achieved via the NOSYM keyword), or alternatively, to perform a least-squares fit on the radical prior to the EPR calculation. This is illustrated in Fig. 18.5a. This method is by far not always valid:

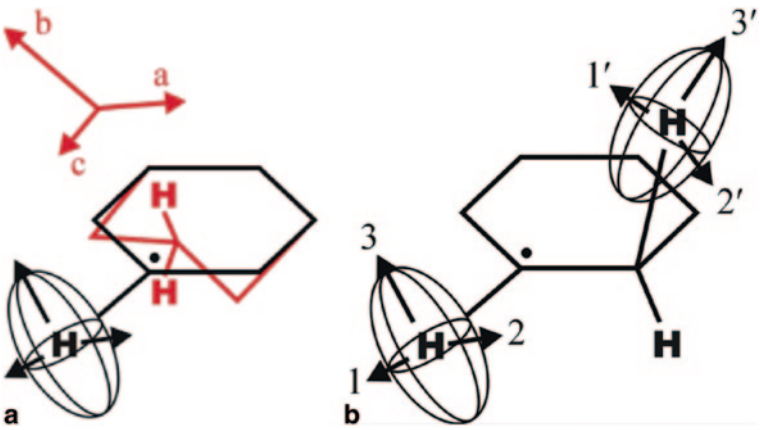

Fig. 18.5 **a** In a single molecule approach, the calculated principal directions of, e.g. a hyperfine tensor in a radical (represented by an *ellipsoid—black*) can be referred to the crystallographic axes <*abc*> by first performing a least-squares fit between the radical structure and the pristine crystal structure (*red*). **b** Alternatively, the relative orientations of the principal directions from two different hyperfine tensors can be used as a measure to compare with experiment: for instance the angles between principal directions *1* and *1′*, *1* and *2′*, and so on

the structure of a radical often differs substantially from the undamaged crystal structure. In several radiation-induced carbohydrate radicals, for example, the ring structure is dramatically broken up (see Chap. 6).

Another way to cope with the unavailability of the crystal axes' orientation in the single molecule approach is to consider the relative orientations of two or more EPR spectroscopic properties (see Fig. 18.5b). The angles can be determined between the principal directions (1, 2, 3) of one hyperfine coupling tensor and those (1′, 2′, 3′) of another hyperfine tensor, or the g-tensor. The resulting data matrix can then be compared to that determined in a similar fashion for the experimental data. Yet, application of this complex procedure to identify radiation-induced radicals in fructose has worked out rather disappointingly. The structure predicted in this way [47] for the most abundant room-temperature stable radical was later shown to be not correct [35]. An absolute analysis of the principal directions of hyperfine and g-tensors remains preferential, unless of course there is no direct link to the crystallographic axes in the experiment itself. This is frequently the case in EPR studies of biomolecules (e.g. proteins) where crystals are hard to grow and measurements are much easier to perform in powders or frozen solution. In that case, a relative analysis of the principal directions does make sense [38, 41].

As stated, the model space is the single most important computational parameter. Its impact should never be underestimated, especially not in favor of other, more technical parameters such as the density functional or extent of the basis set. Although the latter parameters are obviously of importance and of interest, I do not believe that any novelty density functional or extended basis set can make up for the neglect of the molecular environment in, e.g. a single molecule approximation

of what would be a condensed-phase molecular system. In a nutshell: efforts should first go to providing a sufficient computational description of the model space; only then should other parameters be contemplated. In line with that view, a periodic approach is always followed throughout this chapter, usually with triple-ζ basis sets [25, 29] and the BLYP functional [22, 23].

18.2.5 Temperature

Usually, the calculations in the 'structure manipulation' and 'EPR calculation' steps (see Fig. 18.1) are static. That is, only one radical conformation is considered, typically one obtained from an energy minimization. These algorithms (e.g. LBFGS [21]) do not guarantee that the resulting conformation is effectively the global energetic minimum on the potential energy surface in terms of all possible degrees of freedom. They are only able to locate a minimum, possibly a local one. This is illustrated in Fig. 18.6 where, starting from an initial structure (black circle) the algorithm drops into the nearest local minimum (black cross), instead of the central global energetic minimum. Hence, static structure manipulation calculations could result in a 'wrong' conformation, and the ensuing radical model identification might be equally erroneous.

But even when the 'correct' radical conformation is obtained, a static EPR calculation on this one conformation only does not exactly correspond to reality either. From a methodological point of view, this amounts to simulating the radical at 0 K, whereas experimental measurements on the radical occur at a finite temperature. And in reality, the radical and its environment undergo rapid conformational changes that do affect the spectroscopic properties: an average property is measured over a considerable time epoch (of the order of *ms*) during typical EPR experiments, be they continuous wave or pulsed. Therefore, for the hypothetical potential energy surface of Fig. 18.6, the observed EPR properties will be the Boltzmann-weighted average of the spectroscopic properties for all three minima. Those of the central, global minimum will certainly dominate, but the properties of the local minima will contribute as well.

Going beyond the static approximation in a computational approach is possible by using, e.g. molecular dynamics (MD) in which Newton's equations of motion are solved iteratively. In a series of consecutive discrete timesteps (typically 1 fs), the atomic coordinates of a radical model evolve in time. For each step, the force due to the potential energy (calculated at the DFT level of theory) and a kinetic energy contribution (finite temperature) is evaluated and integrated. This yields a trajectory, an ensemble of snapshots (one for each timestep) that represent the atomic motion of the molecular system during the total simulated time. On current-day High Perfomance Computing facilities, it usually takes several seconds to evaluate the ab-initio forces for a molecular system at one timestep (1 fs). Hence, MD simulations relying on DFT usually span just several *ps* or *ns* only. The effective calculation time for such a simulation often takes several weeks or even months!

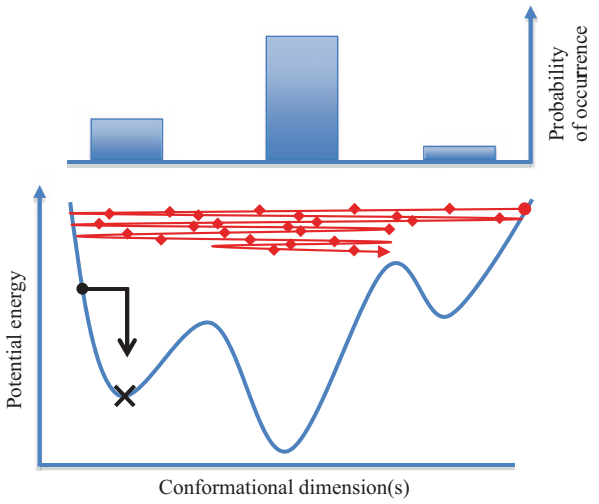

Fig. 18.6 Illustration of a (fictitious) *potential energy* surface and the effect of an energy minimization algorithm (in *black*) and molecular dynamics (in *red*)

Relying on MD as the main algorithm in the 'structure manipulation' step offers the possibility to locate new, more stable minima. Even when a poor initial conformation is chosen (e.g. the red sphere in Fig. 18.6), a large part of the multidimensional potential energy can still be reached: the introduction of kinetic energy enables that barriers in the potential energy surface can be crossed. Sufficiently long MD simulations, then, allow complete sampling of the potential energy surface. More optimal conformations will occur more during the trajectory, with their probability of occurrence directly (but inversely) related to their potential energy (illustrated at the top of Fig. 18.6).

An MD trajectory can also be used to account for temperature effects on the calculated EPR properties. Instead of determining these for just one conformation (e.g. the black cross in Fig. 18.6), a whole bunch of conformations attained during the MD can be considered. Usually, a subsampling of the trajectory is used—100–1000 snapshots (e.g. the red diamonds in Fig. 18.6)—for which the EPR properties are each time calculated. Subsequently, the resulting data is averaged. This is straightforward for scalar data, such as the isotropic hyperfine coupling tensor, but for other tensorial data care should be taken that diagonalization is only performed after the averaging.

If EPR properties are calculated for N snapshots from an MD trajectory, the average hyperfine coupling tensor (for example) is:

$$\langle \mathbf{A} \rangle = \frac{1}{N} \sum_{i=1}^{N} \mathbf{A}_i \tag{18.1}$$

Subsequently, this average tensor is diagonalized:

$$\begin{pmatrix} \mathbf{V}_1 & \mathbf{V}_2 & \mathbf{V}_3 \end{pmatrix}^T \langle \mathbf{A} \rangle \begin{pmatrix} \mathbf{V}_1 & \mathbf{V}_2 & \mathbf{V}_3 \end{pmatrix} = \begin{bmatrix} A_1 & & \\ & A_2 & \\ & & A_3 \end{bmatrix} \tag{18.2}$$

This yields three average eigenvalues $A_1 - A_3$ (expectation values) and their corresponding principal directions $V_1 - V_3$. The same procedure can obviously be used for the g tensor.

Although temperature does affect the calculated EPR properties, the effect is usually quite subtle for solid-state radicals. Solvated radicals are much more flexible (e.g. [49]) than those trapped inside a crystalline matrix, with concomitant effect on their spectroscopic properties. In fact, static EPR calculations usually suffice for structural identification purposes. The added value of dynamic calculations is that insight is obtained in the structural dependence of the spectroscopic properties involved. For instance, in the main α-type glycine radical, out-of-plane motion of the paramagnetic center has a marked effect on the hyperfine coupling tensor of the associated α-carbon and α-proton (e.g. [40, 42]).

18.2.6 Case Study 2: Sucrose Radicals T2/T3

The radicals that are stable at room temperature in irradiated sucrose have been elaborately characterized by De Cooman et al. in joint experimental-computational studies [8, 10, 11]. Three different radicals are present in the irradiated crystalline matrix, labeled T1, T2 and T3. The latter two radicals are very similar, as can be seen from their spectroscopic properties (Table 18.3), and both were identified as having the same chemical structure. The origin of the minor differences in spectroscopic properties for both radicals is still unclear, although it is suspected that changes in the molecular environment might be the cause [8, 10, 11].

The structure of the T2/T3 radicals is shown in Fig. 18.7. Considerably more than simple hydrogen abstraction has occurred: the glycosidic linkage between the glucose and fructose unit is broken, a carbonyl group is present at C2 and the unpaired electron is localized at C1. In the original publication [8], this structure was identified from a limited set of plausible radical models that was first obtained by adopting the point-dipole approximation. Subsequent DFT calculations, relying on the CPMD software [50] for periodic structure calculations and ensuing cluster calculations with Gaussian [48], yielded the conclusive identification.

Repeating the identification in a uniform periodic approach with the aid of CP2K [6] and the same computational parameters mentioned in paragraph 18.2.2, at first an initial geometry is generated starting from the crystallographic unit cell. The H2 and HO2 hydrogens are removed, and an additional proton is placed at the O1 position. The C1–O1 bond is broken during the energy minimization, by applying a restraint force keeping both atoms apart, followed by an unrestrained minimization. The structure resulting from this rather straightforward approach, in line with that in the previous showcase, is shown in Fig. 18.8a and will be referred to as radical model M(T2/T3-a).

Calculated EPR properties for this radical model are given in Table 18.4 and the nice agreement with the experimental properties of Table 18.3 is immediately clear. The proton at C1 gives rise to an α-type hyperfine coupling, the other couplings are due to γ-protons H(C3) and H(C5). Even though the size of the isotropic coupling

Table 18.3 Overview of EPR properties for radical species T2/T3 (taken over from Ref. [8]). Principal directions are given with respect to the orthogonal <a*bc> reference frame. Although g-tensor information is also available [10], the focus in this chapter will be on the hyperfine coupling tensors

Coupling	A_{iso}	A_{aniso}	Principal directions		
T2					
Hα	−38.69	−19.66	0.424	−0.163	−0.891
		−2.11	0.886	0.280	0.371
		21.77	0.189	−0.946	0.263
Hβ1	16.37	−2.32	0.869	−0.355	−0.344
		−1.72	−0.209	0.368	−0.906
		4.04	0.448	0.86	0.246
Hβ2	13.68	−3.09	0.718	−0.65	0.248
		−2.17	0.638	0.473	−0.608
		5.26	0.278	0.595	0.754
T3					
Hα	−35.81	−18.98	0.584	−0.184	−0.79
		−2.11	0.755	0.481	0.446
		21.09	0.298	−0.857	0.420
Hβ1	16.42	−2.1	0.84	−0.541	−0.034
		−1.77	0.178	0.334	−0.926
		3.87	0.512	0.772	0.377
Hβ2	12.24	−3.62	0.528	−0.822	0.214
		−2.12	0.804	0.402	−0.439
		5.74	0.275	0.403	0.873

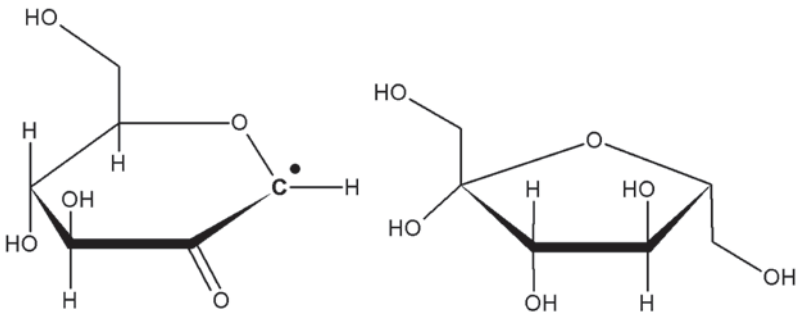

Fig. 18.7 Molecular structure for radicals T2/T3, identified by De Cooman et al. in [8]

for H(C1) is slightly underestimated in the calculations, this agreement can still be considered as very good, especially considering the agreement between the corresponding principal directions: calculated and measured eigenvectors align to within ~10° for radical T3 and even less than 5° for radical T2. These calculations yield similar results as those of the cluster calculations by De Cooman et al. [8], although there slightly better isotropic values were obtained (possibly owing to the use of the B3LYP functional [51] in the EPR calculation step).

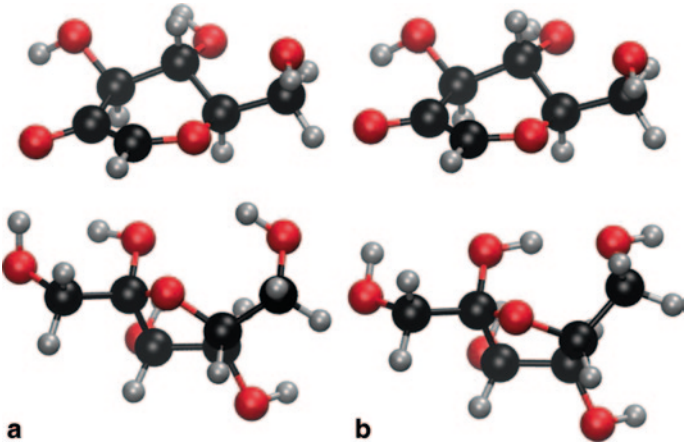

Fig. 18.8 Conformation of the radical models corresponding to measured radicals T2/T3: **a** M(T2/T3-a) after 'simple' energy minimization starting from the adapted crystallographic unit cell structure. **b** M(T2/T3-b) after energy minimization ensuing an 11 ps MD run. 3D-renders produced with the aid of VMD [20]

To go beyond this static approach, ab initio MD simulations are initiated on the optimized structure of radical model M(T2/T3-a). Simulations are performed in the NVT ensemble, employing a time step of 1 fs for a total of 11,000 steps (11 ps). A fast velocity-rescaling thermostat algorithm [52] is used in the first 1000 steps, after which the Nosé-Hoover thermostat [53, 54] is selected for the final 10 ps (which are considered of *production* quality). An illustration of the conformational changes to the radical model is given in Fig. 18.9, where several snapshots throughout the production part of the MD trajectory are shown.

In the glucose unit, mostly the planarity of the radical center (C1) changes as it undergoes an umbrella-like motion. In the fructose unit, the position changes of the hydroxyl proton on oxygen O1 (which constituted the former glycosidic linkage). The former molecular motion can be quantified to some extent by the *improper* dihedral angle H(C1)–C2–O5–C1, the latter molecular motion by the dihedral angle H(O1)–O1–C2′–C3′. The variation of these two angles throughout the MD trajectory is shown in Fig. 18.10.

The conformation of the radical center (blue) remains planar on average, but out-of-plane digressions of about −20°/+20° occur due to the umbrella-like motion. The orientation of the hydroxyl proton on oxygen O1 (red) changes by 60° after about 2 ps in the MD: clearly a new, stable conformation is obtained. This is confirmed when the last snapshot from the MD trajectory is subject to full energy minimization. The resulting conformation M(T2/T3-b), shown in Fig. 18.8, has an absolute energy of −513.57366 a.u. which is lower by about 35 kJ/mol than that of conformation M(T2/T3-a) at −513.56042 a.u.

The EPR properties of this new energetic minimum M(T2/T3-b) are quite similar to those of the other conformation (see Table 18.4). The isotropic hyperfine coupling values for protons H(C3) and H(C5) are slightly raised, but the anisotropic parts have hardly changed and the principal directions are roughly in the same direction as for

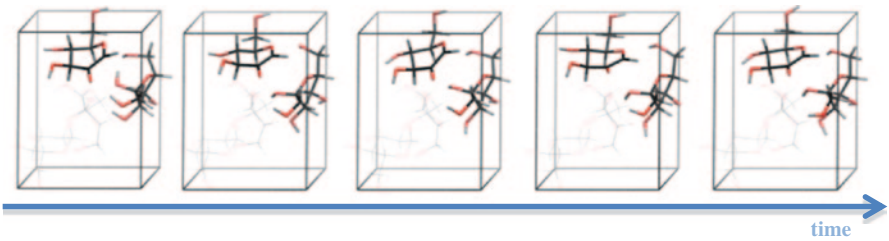

Fig. 18.9 Conformations of radical M(T2/T3) representatively sampled throughout the last 10 ps of the MD simulation. 3D-renders produced with the aid of VMD [20]

Table 18.4 Calculated EPR properties for radical models M(T2/T3-a) and M(T2/T3-b). Isotropic (A_{iso}) and anisotropic hyperfine couplings (A_{aniso}) are in MHz. The angle (in degrees) indicates the agreement in direction between the calculated eigenvectors and those of the experimental tensors of radicals T2 and T3, respectively (see Table 18.3)

Atom	A_{iso}	A_{aniso}	Angle (T2)	Angle (T3)	Coupling
M(T2/T3-a)					
H(C1)	−23.20	−16.91	1.1	9.9	Hα
		−4.99	4.6	10.5	
		21.90	4.5	8.3	
H(C3)	21.04	−2.19	7.7	14.3	Hβ1
		−1.85	7.8	14.7	
		4.04	2.3	8.7	
H(C5)	13.44	−3.26	14.7	24.5	Hβ2
		−1.72	16.3	24.5	
		4.99	12.0	1.0	
M(T2/T3-b)					
H(C1)	−24.65	−15.88	2.5	9.3	Hα
		−4.76	5.9	9.9	
		20.64	6.3	6.0	
H(C3)	24.00	−2.38	1.7	21.4	Hβ1
		−1.63	8.9	21.4	
		4.01	9.0	1.0	
H(C5)	15.80	−3.49	13.0	21.5	Hβ2
		−1.81	14.4	21.5	
		5.30	13.1	0.3	

conformation M(T2/T3-a). This can be expected, since the main changes between both conformations have not happened to the radical center itself but merely in its vicinity. Accordingly, one cannot easily state that one conformation or the other agrees better with experimental data. But given that it has a lower potential energy, conformation M(T2/T3-b) is much more likely to correspond with reality.

So far still, the EPR properties were calculated in a *static* fashion: for one conformation only (even though its structure might have sprung from a dynamic simulation). To go beyond that, EPR properties are calculated for 1000 snapshots, regularly sampled (every 10 fs) during the last 10 ps of the MD simulation. The variation of the spectroscopic properties is illustrated in Fig. 18.11, where the isotropic hyper-

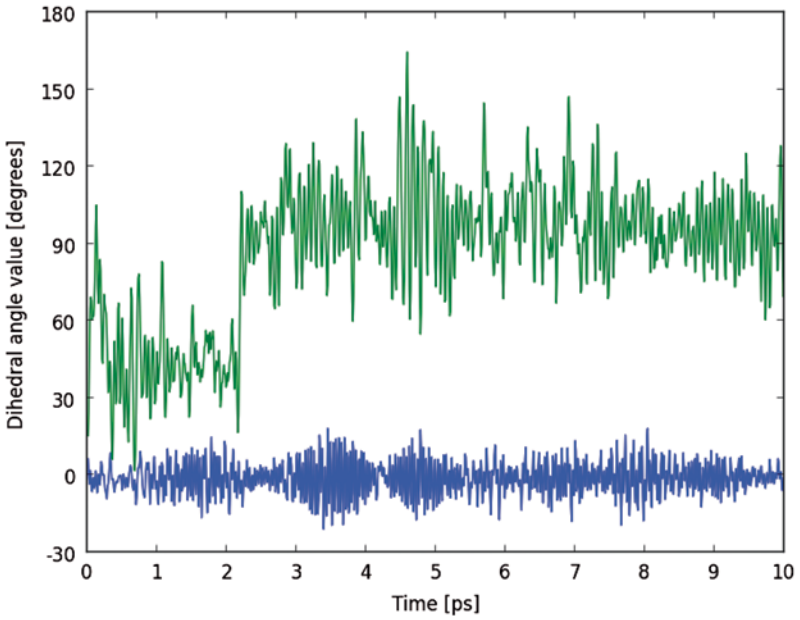

Fig. 18.10 Variation of *dihedral angles* H(C1)–C2–O5–C1 (*blue*) and H(O1)–O1–C2′–C3′ (*green*) in sucrose radical model M(T2/T3) during the last 10 ps of an MD simulation at 300 K

fine coupling values of H(C1), H(C3) and H(C5) are plotted as a function of simulation time.

The isotropic couplings vary considerable as (even minor) conformational changes occur during the MD run. Yet, on average, the values fluctuate about −23.47 MHz for H(C1), 21.11 MHz for H(C3), and 16.51 MHz for H(C5), close to what is found in the static approaches for conformations M(T2/T3-a/b). The variation of the proton coupling values during the dynamics is perhaps best seen in a histogram (Fig. 18.12). This type of plot reverberates the typical experimental EPR spectra, but more importantly gives insight in the "variability" that can be attained in a prototypical computational approach. For the H(C1) α-type coupling, the isotropic value easily covers the interval −30 to −20 MHz. The variability for the γ-type couplings H(C3) and H(C5) is even bigger. Here, the dispersion in values can be of the 20 MHz order. Note that this is not an "error" nor standard deviation for the computational setup; this analysis merely indicates how susceptible the calculated EPR properties are to (minor) conformational changes during the molecular dynamics.

To fully analyze the calculated hyperfine tensor data for the snapshots from the MD simulation, an average tensor is calculated according to Eqs. (18.1)–(18.2). To distinguish the possible effect of the H(O1) hydroxy proton rearrangement (see Fig. 18.10) on the calculated EPR properties, average hyperfine tensors are calculated for three time epochs: one for the snapshots in the time range 0.00–2.25 ps, another for the range 2.35–10.00 ps, and another for *all* snapshots from the MD simulation. These results are presented in Table 18.5.

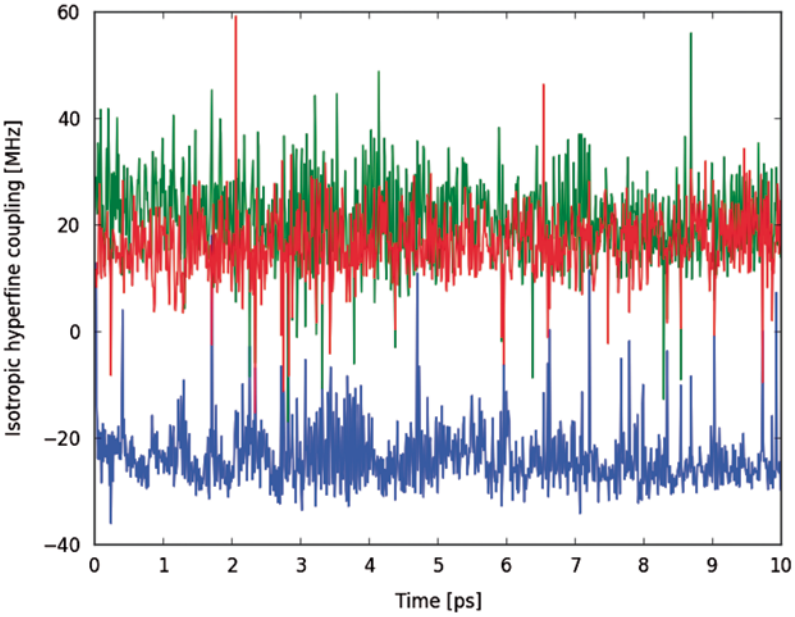

Fig. 18.11 Variation of the *isotropic hyperfine coupling* values (in MHz) of protons H(C1) (in *blue*), H(C3) (in *green*), H(C5) (in *red*) for sucrose radical model M(T2/T3) during a 10 ps MD simulation at 300 K

There are no major differences between the average hyperfine tensors for the three time epochs. Isotropic and anisotropic values differ by 1 MHz at most, eigenvector directions change by merely a couple of degrees. Clearly, the hydroxy proton rearrangement in the vicinity of the radical has no significant influence on the EPR properties, in line with the observations on the static calculations for conformations M(T2/T3-a and b). Furthermore—and unfortunately—the hydroxy proton conformational change cannot explain the difference in spectroscopic properties between T2 and T3.

From a comparison between the results in Tables 18.4 and 18.5 (e.g. those for all snapshots in the MD), it can be concluded that the dynamic treatment does not yield a better agreement with experiment than the static approach. It can give insight, however, into which molecular motions modulate the hyperfine coupling tensor. α-type tensors (such as that for H(C1)) are known to depend near-quadratically on the planarity of the radical center [42]. Although this effect is less pronounced and less clear than in glycine, it is still apparent (with some imagination) from a scatterplot of the isotropic hyperfine coupling versus the radical planarity, as measured by the H(C1)–C2–O5–C1 *improper* dihedral angle (Fig. 18.13).

This showcase illustrates that going beyond a *static* approach to simulate the EPR properties in a *dynamic* fashion is not always necessary, especially if the intention is only to identify a radical structure. But an MD approach may lead to the identification of new conformational minima that are more optimal in energetic terms.

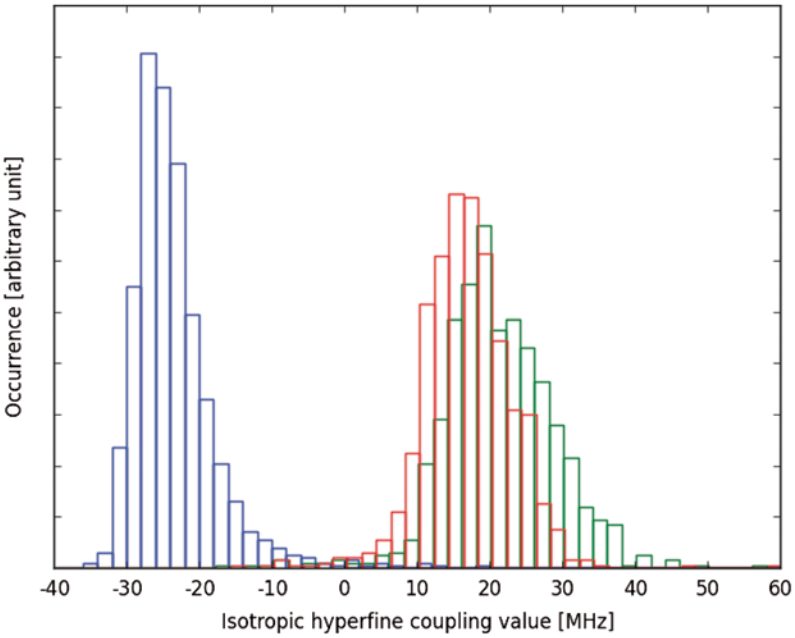

Fig. 18.12 Histograms of isotropic hyperfine coupling values encountered during a 10 ps MD simulation of sucrose radical model M(T2/T3) at 300 K. *Blue*, *green*, and *red boxes*, respectively, indicate the *occurrence* for proton couplings H(C1), H(C3) and H(C5)

18.3 Uncovering Radical Formation—*HOW?* and *WHY?*

18.3.1 General Strategy

Once the structure of a radical has been identified, the obvious question springs to mind: which radiation-induced molecular processes lead up to the formation of this particular radical? Sometimes, as for "simple" hydrogen abstraction products, the underlying radiochemical reactions may seem trivial. For other radicals, that have undergone more elaborate changes with respect to the pristine crystal structure, these processes might be entirely unclear. Yet, caution should always be in place when considering the formation mechanisms of radicals, even when it concerns the "simplest" radiation-induced species. A fine example of this is solid-state alanine. This model system for radiation damage in proteins has attracted numerous studies and its radiation chemistry is commonly considered to be well established [55]. Yet, a recent study [30] has shown that several of the radiation-induced reactions and rearrangements involved were poorly understood, highlighting the value of a computational approach supporting available (experimental) data.

An even more fundamental question that is raised when the identity and formation of a specific radical have been established is: why is this particular radical formed as a result of irradiation? Consider the example of a model decamer DNA

Table 18.5 Time-averaged hyperfine coupling tensors for sucrose radical model M(T2/T3) for various parts of the MD simulation. Isotropic (A_{iso}) and anisotropic hyperfine couplings (A_{aniso}) are in MHz. ψ(T2) and ψ(T3) indicate the angles (in degrees) between the calculated eigenvectors and those of the experimental tensors of radicals T2 and T3, respectively (see Table 18.3)

Atom	Average (0.00–2.25 ps)				Average (2.35–10.00 ps)				Average (0.00–10.00 ps)				Coupling
	A_{iso}	A_{aniso}	ψ(T2)	ψ(T3)	A_{iso}	A_{aniso}	ψ(T2)	ψ(T3)	A_{iso}	A_{aniso}	ψ(T2)	ψ(T3)	
H(C1)	−22.77	−15.27	2.3	8.6	−23.73	−15.52	1.9	10.9	−23.47	−15.44	1.6	10.2	Hα
		−4.37	7.1	8.3		−4.15	3.4	11.3		−4.20	4.3	10.5	
		19.64	6.9	6.1		19.67	3.6	10.5		19.64	4.1	9.5	
H(C3)	23.27	−2.33	9.0	13.0	20.47	−2.25	2.8	18.1	21.11	−2.26	5.0	16.1	Hβ1
		−1.49	10.1	12.4		−1.61	2.7	19.9		−1.59	5.1	17.3	
		3.82	5.0	6.3		3.86	0.6	9.6		3.85	1.1	8.6	
H(C5)	15.61	−3.11	10.6	16.7	16.87	−3.12	11.5	19.5	16.51	−3.10	11.2	18.5	Hβ2
		−1.87	11.4	16.7		−1.69	10.0	20.1		−1.74	9.8	18.8	
		4.98	13.6	0.8		4.80	9.5	4.8		4.84	10.6	3.6	

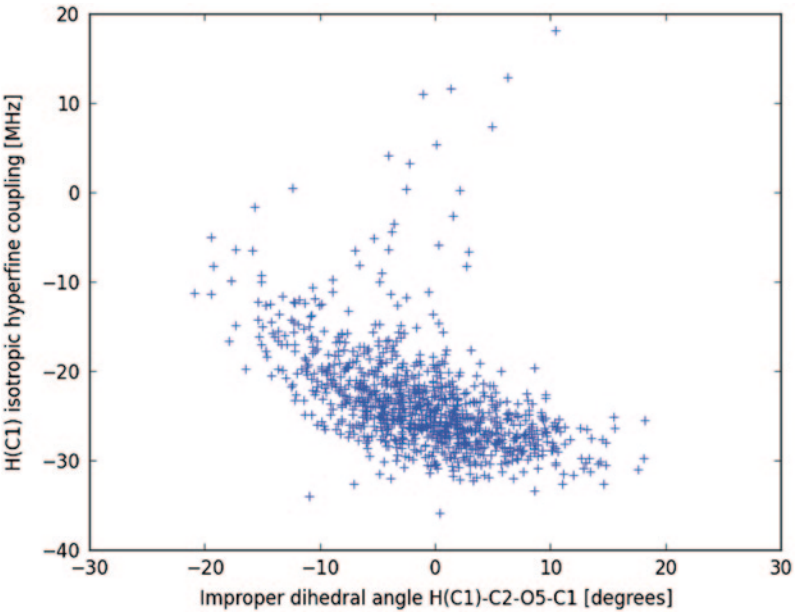

Fig. 18.13 Variation of the *H(C1) isotropic hyperfine coupling* value as a function of the radical planarity, measured by the *improper dihedral angle H(C1)–C2–O5–C1*, for 1000 snapshots sampled from a 10 ps MD simulation at 300 K of sucrose radical model M(T2/T3)

system [56] in which a main radiation-induced radical was identified as being deprotonated at one specific carbon in the deoxyribose sugar subunit of a guanine base. The regioselectivity involved is very intriguing: four other similar carbon centers are present in the sugar at which site deprotonation could occur. To date, no satisfying explanation for this regioselective action of radiation has been presented, for the model DNA system, or for various other biomolecular systems. Here, as well, a computational approach can be of assistance.

Molecular modeling, and DFT methods in particular, can be applied to gain insight in (radio)chemical reactions [57]. Once stationary points have been found and characterized for the reactant and product states, the structural rearrangements that transform one into the other can be determined by mapping all elementary steps along the reaction coordinate(s). Hence, by shedding light on the conformational changes, these methods can help to solve the *HOW?* question. The variation of the (potential) energy along this reaction path, or the energy difference between key points along that path, can assist in solving the *WHY?* question.

This is illustrated in Fig. 18.14 for a hypothetical (potential) energy surface. Once stationary points **A** and **B** have been identified, molecular modeling algorithms allow the characterization of the pathway connecting both states. From that, the changes in the conformational dimensions can be deduced, indicating *how* conformation **A** transforms into conformation **B** and what the nature is of the transition state connecting both minima. At the same time, the changes in energy along the

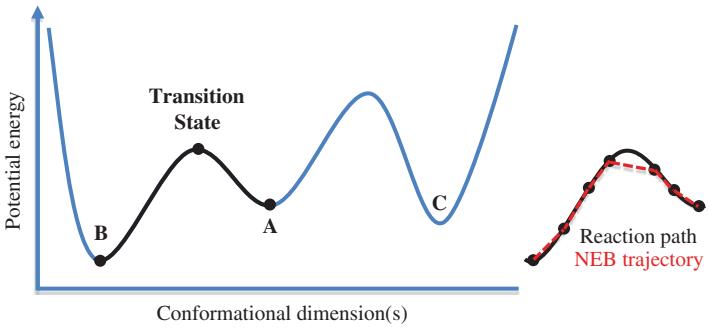

Fig. 18.14 Hypothetical (potential) energy surface illustrating reaction pathway concepts

path enable an estimation of the barrier height (or activation energy), giving insight in the rate of the transformation. This, together with the absolute (potential) energy differences between conformational states can be applied to rationalize preferential formation. In the hypothetical example of Fig. 18.14, reaction from state **A** towards **B** is preferred over **C**, both thermodynamically as well as kinetically.

Several molecular modeling algorithms exist to characterize reaction pathways, but their usefulness for solid-state systems depends on the implementation and on the desired model space approach. Transition state searches in terms of internal coordinates [58] (e.g. in Gaussian [48]) have been used for single-molecule treatments in amino acids and DNA/RNA sugars [39, 43, 59, 60], but are difficult from a computational point of view in condensed states, due to the multitude in degrees of freedom. Reaction pathway modeling in solid-state systems that are described with a periodic approach can be achieved with the aid of the Nudged Elastic Band (NEB) method [61–63]. In this approach, the minimal energy path between two stable molecular conformations is sought by optimizing the energy of a set of intermediate replicas that represent the gradual transition between both end points and that are successively connected by harmonic springs. This is illustrated in Fig. 18.14 for the path from **A** to **B**, where seven replicas discretize the "true" energy path. Though this method likely yields an underestimate of the actual reaction path, it has been used successfully to get insight in the radiation chemistry of amino acids [64] and sugars [31]. This method will also be applied in this chapter.

When comparing different radiation-induced reaction pathways—in an attempt to solve the *WHY?* question—the stoichiometry involved in those reactions needs to be consistent. This implies that all "waste"-products generated in a radiolysis reaction (e.g. net hydrogen abstraction) are sustained inside the simulation cell. This is certainly a hard requirement in NEB simulations and effectively mimics reality. In a real organic crystal, such abstracted products would diffuse throughout the lattice and either reconnect with another neighboring molecule or remain trapped close to the radical site. Depending on the distance between this reattached or trapped residue and the radiation-induced radical, certain interaction effects can be expected. In a more simplified approach, these radiolysis products are eliminated altogether from the simulation and its energetic contribution assumed to be the same

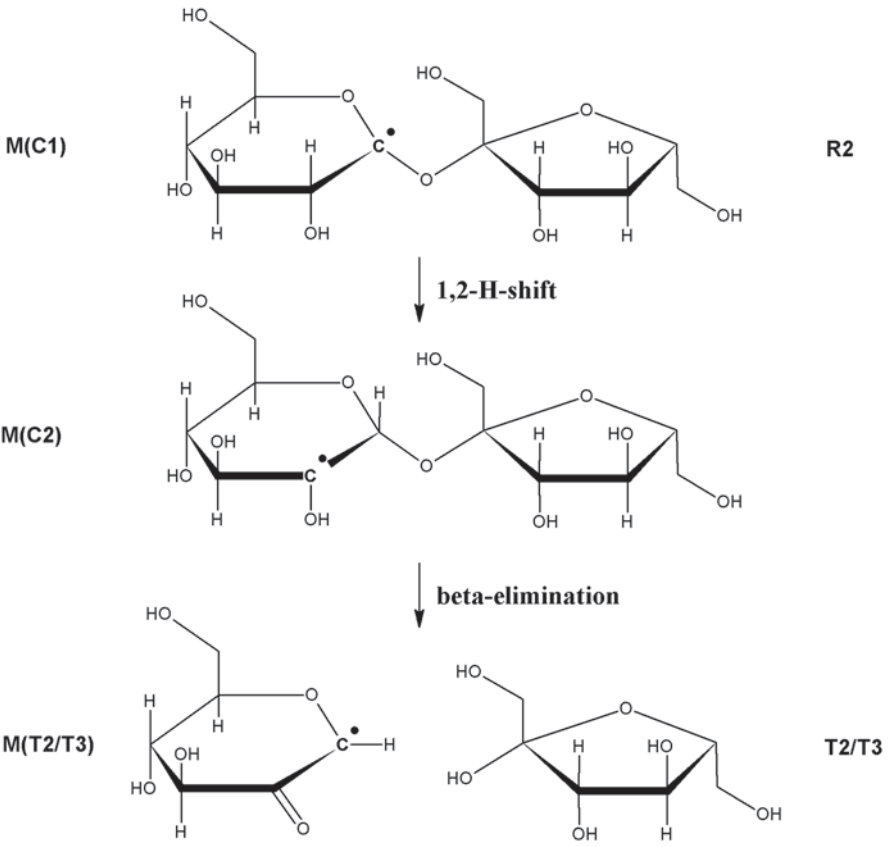

Fig. 18.15 Sucrose radical *R2* (which has only been detected at temperatures below ~100 K) transform into radicals *T2/T3* at room temperature via a *1,2-H-shift* followed by a *beta-elimination* reaction

for a variety of similar radiochemical reactions. Such a methodology is adopted in the determination of, e.g. bond dissociation energies [65], ionization potentials [39, 66] or electron attachment energies [65, 66]. These correspond to very rudimentary reaction pathways, since only the formation energy of a particular radical fragment is considered without looking at barriers encountered. It might nevertheless yield useful information on the selective action of radiation.

18.3.2 Case Study 3: Conversion of Sucrose Radical R2 into T2/T3

A hypothesis put forward by De Cooman et al. [67] is that sucrose radical R2 is a precursor for radical T2/T3. The proposed transformation process (illustrated in Fig. 18.15) involves first a 1,2-H-shift [68, 69], where a hydrogen atom is transferred

from carbon C2 to the adjacent C1. Then, this intermediate species undergoes beta-elimination [68, 69]: the hydroxy proton at O2 is transferred to the oxygen (O1) of the glycosidic linkage, the C1–O1 bond is ruptured and a C2 = O2 carbonyl group is introduced in the glucose subunit of sucrose. The entire process would rationalize the fact that R2 can only be observed at low temperatures. When enough thermal energy is available, energy barriers can be surpassed and the transformation process is initiated, up until T2/T3 species is formed. The driving force is likely the greater stability of the latter radical species, which is consistent with the fact that T2/T3 have only been observed at room temperature.

A computational approach in line with the previous general strategy serves to shed light on this tentative transformation process. Although the full radiation chemistry of sucrose is not explored exhaustively, the new results presented below provide a sufficient treatment of the formation of radical R2 up to the transformation into T2/T3.

Selective Formation of R2-Radical Model M(C1) As reviewed in Sect. 18.2.2, the structure of radical R2 has been positively identified as corresponding to that of radical model M(C1), where a net hydrogen abstraction from carbon C1 in the pristine sucrose structure has occurred. Yet, several other, similar hydrogen abstractions from carbon are possible in the sucrose structure: from C2, C3, C4, C5, C6, C1′, C3′, C4′, C5′ and C6′. Why is abstraction from C1 seemingly favored?

Although the primary effects of radiation damage on a molecular level remain debated, current understanding is that radiation leads to the formation of primary oxidative (one-electron loss) and reductive (one-electron gain) free radicals [69]. Subsequently, these primary species decay and transform into more stable (radical) fragments. In carbohydrates, this is likely achieved by the ejection of a proton or even a hydride anion, which then can diffuse through the crystal lattice or be trapped near the original radical site. To a first approximation, the fate of this ejected proton/hydride can simply be disregarded. This simplifies tremendously a comparison of the formation energies for the various possible radical models. All models share a common reference (the pristine sucrose structure) and preferential formation can be deduced from the relative energy differences between the possible radical models.

Energy minimizations are performed for radical models M(C1) to M(C6′) using the same computational parameters as mentioned in Sect. 18.2.2. The final (potential) energies for these species are compared in Table 18.6. Formation of M(C1) and M(C2) is energetically favored, with slight preference (6 kJ/mol) for the latter. This does not correspond entirely to the findings of low-temperature EPR experiments [9]. In that study, six radical species were found to be generated at low temperature, three of which were structurally identified: radical models M(C1) and M(C6), and an alkoxy radical formed by abstracting a hydrogen from oxygen O3′.

Though the simple energy computations in the present work confirm that M(C1) is among the preferentially formed radical species, they do not explain the observation of M(C6) in the experiment: the energy of M(C6) is 149 kJ/mol higher than that of M(C1), based on which one would expect this radical not to be formed. The computations also don’t explain why radical M(C2) is not observed in experiment. It has the lowest potential energy and would clearly be the most favorably formed species.

Table 18.6 Energy comparison for all radical models where one hydrogen has been abstracted from a carbon in sucrose. The absolute energy of M(C2) is used as reference: −513.5641 a.u.

H-abstraction model	Relative energy (kJ/mol)
M(C1)	6.0
M(C2)	0.0
M(C3)	150.6
M(C4)	152.5
M(C5)	153.7
M(C6)	155.1
M(C1′)	141.7
M(C3′)	163.7
M(C4′)	153.8
M(C5′)	147.1
M(C6′)	142.3

Obviously, the assumptions made in the computations above are flawed and the potential energy only is not a very good approximation of the formation energy. For instance, an abstracted proton or hydride will likely be trapped in a different site when it is ejected from either C1 or C3, or will at least disturb the immediate surrounding of the radical in a different fashion when it diffuses through the lattice. This will have a concomitant effect on the relative (formation) energies (as was already demonstrated in case study 2). The fate of these abstracted atomic or molecular fragments should therefore not be disregarded. Also, it should not necessarily be assumed that a radiochemical formation reaction is thermodynamically controlled. Kinetic control could also be in place, requiring knowledge on the barriers associated with radical formation. Unfortunately, this considerably complicates relative comparison of formation energies since the *HOW?* question should be solved in detail for every radical model contemplated. This approach was used successfully to explain selective alkoxy radical formation in rhamnose crystals [31], but at a substantial computational cost.

So, for now, the question why hydrogen abstraction from C1 is seemingly favored by radiation remains unanswered. In all further calculations, the abstracted hydrogen from C1 is not considered in the simulation cell.

Conversion of M(C1) to M(C2) via 1,2-H-Shift Nevertheless, using M(C1) as a starting point, it is possible to determine the energetic landscape for the reaction pathway subsequent to the initial radiation damage. For that, Nudged Elastic Band simulations are used to determine the minimal energy path between consecutive minima and obtain an estimate of the associated energy profile. Each time, ten replicas are used together with a combined steepest descent—DIIS optimizer [71]. The initial guess for the band is generated by linear interpolation between optimized radical structures. The IT-NEB algorithm [62] is then applied for several cycles, followed by CI-NEB [63] until sufficient convergence is reached. The replica with maximal energy along the NEB path is taken as an approximation to the transition state. The resulting energy path, compounded for all reactions discussed below, is shown in Fig. 18.16.

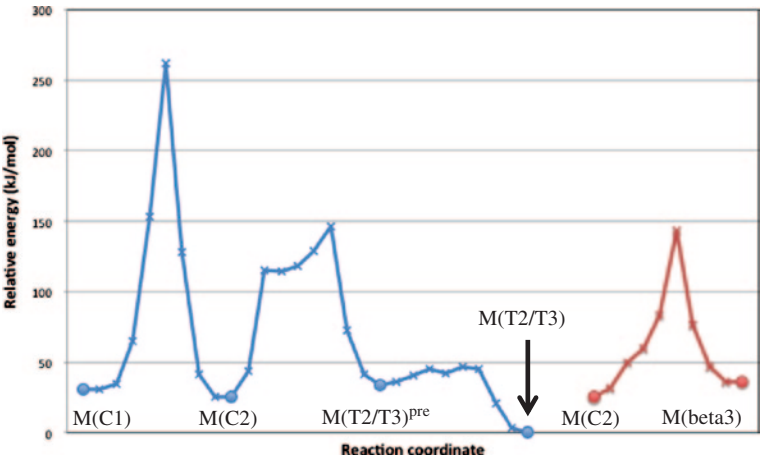

Fig. 18.16 Compound minimal energy path for the radiation-induced transformation pathway of sucrose radical model *M(C1)* into *M(T2/T3)* as obtained from NEB simulations. A competitive transformation path from *M(C2)* to M(beta3) is shown on the *right*. Stationary points are represented by *circles*, intermediate replica along the NEB path by *crosses*. The absolute energy of the *M(T2/T3)* species is used as a reference: −513.5737 a.u.

According to the NEB runs, the 1,2-H-shift from M(C1) to M(C2) is associated with a huge energy barrier, 230 kJ/mol, although this is not unsurpassable considering the energy amount deposited by irradiation. M(C2) has a lower potential energy than M(C1) and so this process is thermodynamically favored. Representative points along the reaction path are shown in Fig. 18.17. Near the transition state, the transferred hydrogen is virtually shared by both carbons C1 and C2. It is not unlikely that this transfer would be assisted by another molecular fragment in the vicinity of that hydrogen, lowering the energy barrier. However, exploratory computational runs in this respect have not yielded any candidates: certainly hydroxyl groups in the vicinity are not prone for such an interaction.

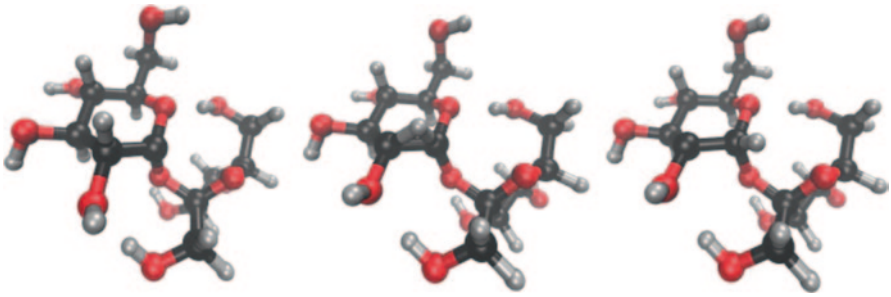

Fig. 18.17 Molecular structure of representative points along the energy path from sucrose radical model M(C1) to M(C2) via a 1,2-H-shift reaction. *Left* M(C1). *Center* near the transition state. *Right* M(C2). 3D-renders produced with the aid of VMD [20]

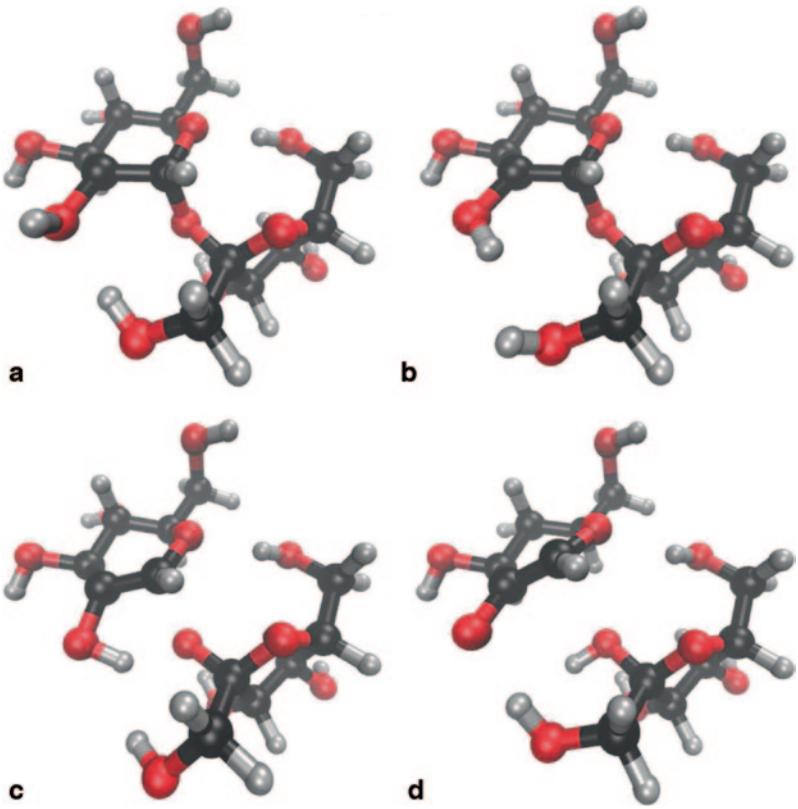

Fig. 18.18 Molecular structure of representative points along the energy path from sucrose radical model M(C2) to M(T2/T3)^{pre} via a beta-elimination reaction. **a** M(C2), **b** O2 hydroxyl group reorientation, **c** proton transfer to O1 and C1–O1 bond rupture, **d** local energetic minimum M(T2/T3)^{pre}. 3D-renders produced with the aid of VMD [20]

Conversion of M(C2) to M(T2/T3) via Beta-Elimination Once M(C2) is generated, it can convert into M(T2/T3) but several molecular rearrangements need to occur, illustrated in Figs. 18.18 and 18.19.

Before the hydroxy proton on O2 can come near the O1 oxygen of the glycosidic linkage, it needs to reorient. In model M(C2) (and in the pristine crystal structure), the proton of O2 is involved in a hydrogen bond to oxygen O6′ of an adjoining sucrose molecule in the lattice. This hydrogen bond is broken when the O2 hydroxyl group reorients, but a new hydrogen bond is almost immediately made with O1′ of the radical (compare structures (a) and (b) in Fig. 18.18). These concomitant reorientations give rise to a considerable barrier: the first cusp in Fig. 18.16 corresponds to structure (b) and is almost 90 kJ/mol higher in energy than M(C2).

Subsequent to the reorientation, hydroxy proton H(O2) attaches to the glycosidic oxygen and triggers rupture of the C1–O1 bond, effectively separating the glucose- and fructose subunits in sucrose. The structure near the transition state for this ensuing process is shown in Fig. 18.18c. Although the energy rise is not as much as for the

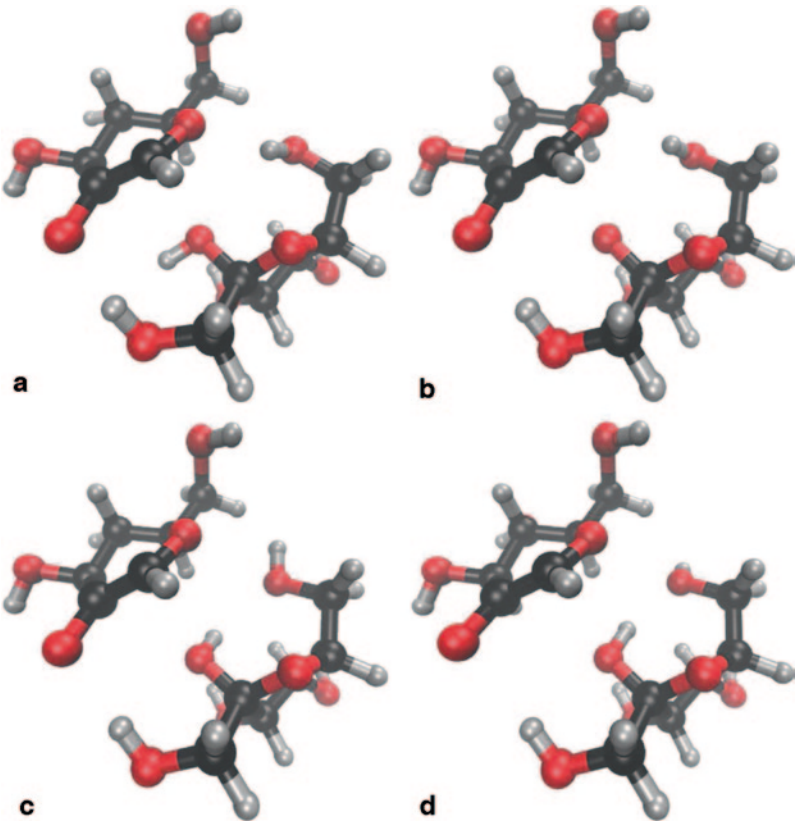

Fig. 18.19 Molecular structure of representative points along the energy path from sucrose radical model M(T2/T3)^{pre} to M(T2/T3). **a** M(T2/T3)^{pre}, **b** O1 hydroxyl group reorientation, **c** O6′ hydroxyl group reorientation, **d** M(T2/T3). 3D-renders produced with the aid of VMD [20]

hydroxyl rearrangement, the total energy barrier for rearrangement and bond rupture is at ~125 kJ/mol with respect to the potential energy of M(C2). This barrier should be easily surpassed, since sufficient (thermal) energy is available in the irradiated sucrose crystal after the M(C1) → M(C2) transformation has occurred.

After the C1–O1 bond has been ruptured, a local energetic minimum is obtained: radical model M(T2/T3)^{pre}, corresponding to structure (d) in Fig. 18.18. Its potential energy is actually higher by 9 kJ/mol than that of M(C2). The entire process would therefore not be thermodynamically favored were it not that subsequent hydroxyl reorientations in model M(T2/T3)^{pre}, give rise to a considerable drop in energy to arrive at the final structure M(T2/T3). These conformational rearrangements are illustrated in Fig. 18.19. First, the newly formed hydroxyl group involving oxygen O1 (the former glycosidic oxygen) reorients by almost 180°: its hydroxy proton no longer points towards O1′ but now makes a hydrogen bond with O6′. Concomitantly, the hydroxy proton on O6′ reorients as well, to arrive at the final M(T2/T3) structure. Note that all these conformational changes do not take place in the radical

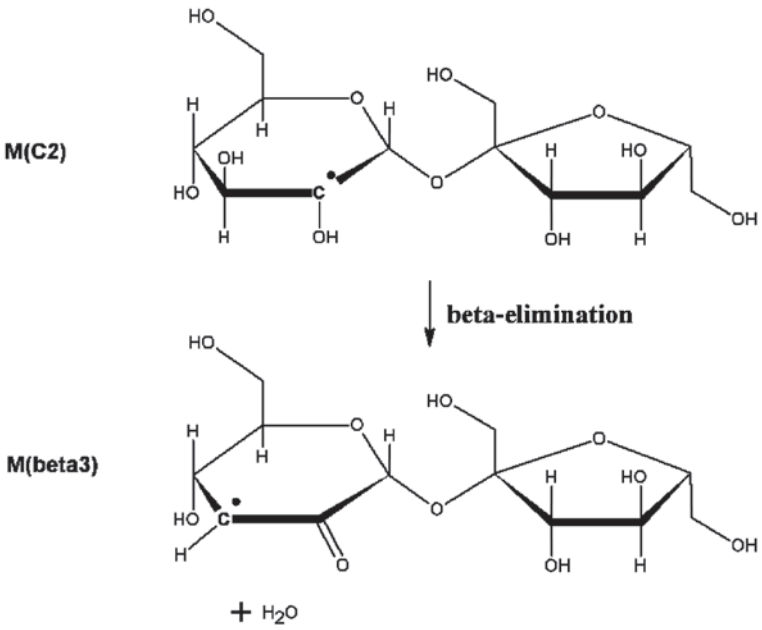

Fig. 18.20 Could a competitive *beta-elimination* reaction from sucrose radical model *M(C2)* lead to the formation of another product *M(beta3)*?

fragment itself (which is in the glucose subunit) but in the fructose subunit, which is in the near vicinity of the radical center. The changes in energy are, however, considerable. After a small barrier (13 kJ/mol) has been passed, the energy quickly drops by 34 kJ/mol between structures M(T2/T3)^{pre} and M(T2/T3).

Total Transformation Process of M(C1) into M(T2/T3) The NEB simulations give unique insight into the conformational changes that occur throughout the overall transformation process of M(C1) into M(T2/T3), and therefore solve the *HOW?* question for this particular process. They also shed light on *WHY?* radicals T2/T3 (corresponding to model M(T2/T3)) can only be observed at room temperature. The entire transformation process is thermodynamically favored: M(T2/T3) is 30.6 kJ/mol lower in potential energy than M(C1). However, the 1,2-H-shift associated with the M(C1) to M(C2) conversion constitutes the rate determining step, with a significant energy barrier of 230 kJ/mol. Enough thermal energy needs to become available in the sucrose crystal, before this process can proceed. But, once this particular barrier has been surpassed, all subsequent transformation steps can proceed without further debilitation, and the intermediate radical species encountered throughout this process would not be observed in experiment.

Competitive Beta-Elimination Products from M(C2)? In the above, M(T2/T3) was obtained from radical model M(C2) via beta-elimination. Yet, this same mechanism applied to model M(C2) could also lead to another radical M(beta3), as outlined in Fig. 18.20. However, this species has not been detected in experiment,

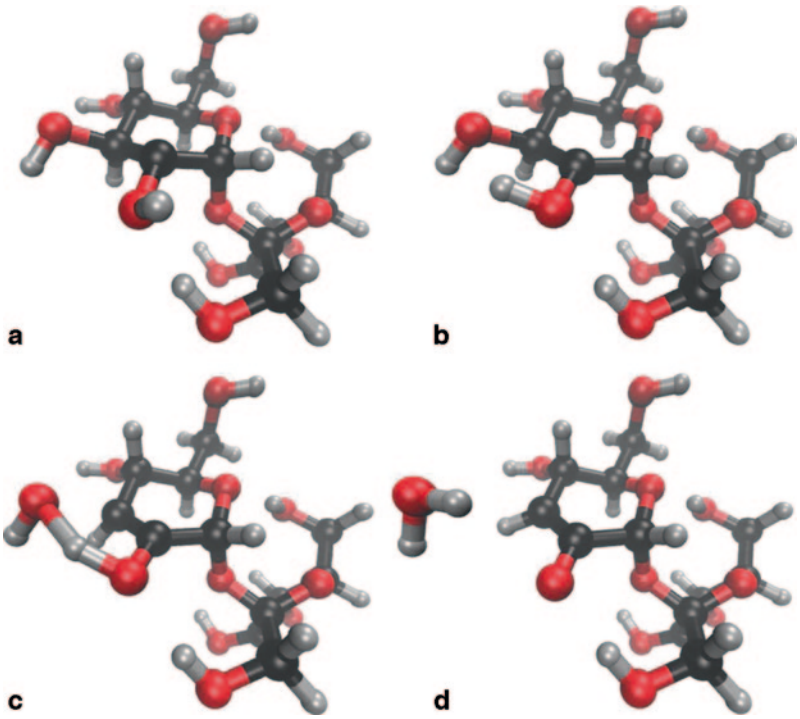

Fig. 18.21 Molecular structure of representative points along the energy path from sucrose radical model M(C2) to M(beta3) via a beta-elimination reaction. (a) corresponds to M(C2), (d) to radical model M(beta3). (b) and (c) are intermediate points 3D-renders produced with the aid of VMD [20]

at low temperature nor at room temperature. Could NEB simulations give insight into why this species is not formed, or rather, why formation of radical M(T2/T3) is favored over M(beta3)?

Representative snapshots along the NEB reaction path are shown in Fig. 18.21. In this beta-elimination reaction, the hydroxy proton on O2 approaches oxygen O3 and connects to it. This causes rupture of the C3–O3 bond and a water molecule is formed. In radical model M(beta3), this molecule remains in the vicinity of the radical (see Fig. 18.21d). The variation of the energy throughout the NEB path is also included in Fig. 18.16 (in red). The barrier is similar in height to that between M(C2) and M(T2/T3), but it is clear that formation of M(beta3) is not advantageous from a thermodynamical point of view: the potential energy of M(beta3) is 11 kJ/mol higher than that of M(C2).

Although in this particular example, all possible transformation processes have not been exhaustively explored, it is clear by far that the energy landscape really dictates the transformation process. By exploring these pathways via NEB simulations, it is possible to gain insight into preferential formation pathways ensuing

radiation damage to biomolecules, and so, solve the *WHY?* question along with the *HOW?* question.

Acknowledgments This work is supported by the Fund for Scientific Research—Flanders (FWO) and the Research Board of the Ghent University. All computational resources (Stevin Supercomputer Infrastructure) and services used in this work were provided by Ghent University, the Hercules Foundation and the Flemish Government—department EWI. This chapter is dedicated to children lost.

References

1. Lund A, Shiotani M (2010) EPR of free radicals in solids: trends in methods and applications. Springer, Dordrecht
2. Heller C, McConnell HM (1960) Radiation damage in organic crystals. ii. electron spin resonance of (CO2H)CH2CH(CO2H) in β-succinic acid. J Chem Phys 32:1535–1540. doi:10.1063/1.1730955
3. McConnell HM (1956) Indirect hyperfine interactions in the paramagnetic resonance spectra of aromatic free radicals. J Chem Phys 24:764–766. doi:10.1063/1.1742605
4. Close DM, Bernhard WA (1977) INDO Calculations of spin-density distribution in pyrimidine electron adducts. J Chem Phys 66:5244–5245. doi:10.1063/1.433754
5. Kaupp M, Bühl M, Malkin VG (2004) Calculation of NMR and EPR parameters: theory and applications. WILEY-VCH: Weinheim doi:10.1002/3527601678
6. CP2K. http://www.cp2k.org
7. VandeVondele J, Krack M, Mohamed F et al (2005) QUICKSTEP: fast and accurate density functional calculations using a mixed Gaussian and plane waves approach. Comput Phys Commun 167:103–128. doi:10.1016/j.cpc.2004.12.014
8. De Cooman HP, Vrielinck H et al (2008) Identification and conformational study of stable radiation-induced defects in sucrose single crystals using density functional theory calculations of electron magnetic resonance parameters. J Phys Chem B 112:7298–7307. doi:10.1021/jp712004g
9. De Cooman HP, Vrielinck H et al (2010) Oxidation and reduction products of X irradiation at 10 K in sucrose single crystals: radical identification by EPR, ENDOR, and DFT. J Phys Chem B 114:666–674. doi:10.1021/jp909247z
10. De Cooman HK, Kusakovskij J et al (2013) Dominant stable radicals in irradiated sucrose: g tensors and contribution to the powder electron paramagnetic resonance spectrum. J Phys Chem B 117:7169–7178. doi:10.1021/jp400053h
11. De Cooman HP, Vrielinck H et al (2009) ENDOR and HYSCORE analysis and DFT-assisted identification of the third major stable radical in sucrose single crystals X-irradiated at room temperature. Phys Chem Chem Phys 11:1105–1114. doi:10.1039/b816641b
12. Vanhaelewyn G, Pauwels E, Callens FJ et al (2006) Q-band EPR and ENDOR of low temperature X-irradiated beta-D-fructose single crystals. J Phys Chem A 110:2147–2156. doi:10.1021/jp056632v
13. De Cooman HV, Pauwels E et al (2008) Radiation-induced radicals in glucose-1-phosphate. I. Electron paramagnetic resonance and electron nuclear double resonance analysis of in situ X-irradiated single crystals at 77 K. J Phys Chem B 112:15045–15053. doi:10.1021/jp804290e
14. Krivokapić A, Øhman KT, Nelson WH et al (2009) Primary oxidation products of 5-methylcytosine: methyl dynamics and environmental influences. J Phys Chem A 113:9633–9640. doi:10.1021/jp904747j

15. Øhman KT, Sanderud A, Hole EO, Sagstuen E (2006) Single crystals of L-O-serine phosphate X-irradiated at low temperatures: EPR, ENDOR, EIE, and DFT studies. J Phys Chem A 110:9585–9596. doi:10.1021/jp061265o
16. Declerck R, Pauwels E, Van Speybroeck V, Waroquier M (2006) First-principles calculations of hyperfine parameters with the Gaussian and augmented-plane-wave method: application to radicals embedded in a crystalline environment. Phys Rev B 74:8. doi:245103 10.1103/PhysRevB.74.245103
17. Weber V, Iannuzzi M, Giani S et al (2009) Magnetic linear response properties calculations with the Gaussian and augmented-plane-wave method. J Chem Phys 131:11. doi:014106 10.1063/1.3156803
18. Pauwels E, Van Speybroeck V, Waroquier M (2004) Evaluation of different model space approaches based on DFT to examine the EPR parameters of a radiation-induced radical in solid-state alpha-glycine. J Phys Chem A 108:11321–11332. doi:10.1021/jp049251a
19. Hermosilla L, Calle P, de la VJMG, Sieiro C (2006) Density functional theory study of N-14 isotropic hyperfine coupling constants of organic radicals. J Phys Chem A 110:13600–13608. doi:10.1021/jp064900z
20. Humphrey W, Dalke A, Schulten K (1996) VMD: visual molecular dynamics. J Mol Graph 14:33–38, 27–28. doi:10.1016/0263-7855(96)00018-5
21. Byrd RH, Lu PH, Nocedal J, Zhu CY (1995) A limited memory algorithm for bound constrained optimization. SIAM J Sci Comput 16:1190–1208. doi:10.1137/0916069
22. Becke AD (1988) Density-functional exchange-energy approximation with correct asymptotic-behavior. Phys Rev A 38:3098–3100
23. Lee CT, Yang WT, Parr RG (1988) Development of the Colle-Salvetti correlation-energy formula into a functional of the electron-density. Phys Rev B 37:785–789
24. Lippert G, Hutter J, Parrinello M (1997) A hybrid Gaussian and plane wave density functional scheme. Mol Phys 92:477–487
25. VandeVondele J, Hutter J (2007) Gaussian basis sets for accurate calculations on molecular systems in gas and condensed phases. J Chem Phys 127:9. doi:114105 10.1063/1.2770708
26. Goedecker S, Teter M, Hutter J (1996) Separable dual-space Gaussian pseudopotentials. Phys Rev B 54:1703–1710
27. Hartwigsen C, Goedecker S, Hutter J (1998) Relativistic separable dual-space Gaussian pseudopotentials from H to Rn. Phys Rev B 58:3641–3662
28. Krack M, Parrinello M (2000) All-electron ab-initio molecular dynamics. Phys Chem Chem Phys 2:2105–2112
29. Godbout N, Salahub DR, Andzelm J, Wimmer E (1992) Optimization of gaussian-type basis-sets for local spin-density functional calculations. 1. Boron through neon, optimization technique and validation. Can J Chem Can Chim 70:560–571
30. Pauwels E, De Cooman H, Waroquier M et al (2010) On the identity of the radiation-induced stable alanine radical. Phys Chem Chem Phys 12:8733–8736. doi:10.1039/c004380j
31. Aalbergsjo SG, Pauwels E, De Cooman H et al (2013) Structural specificity of alkoxy radical formation in crystalline carbohydrates. Phys Chem Chem Phys 15:9615–9619. doi:10.1039/c3cp50789k
32. Pauwels E, Declerck R, Van Speybroeck V, Waroquier M (2008) Evidence for a Grotthuss-like mechanism in the formation of the rhamnose alkoxy radical based on periodic DFT calculations. Radiat Res 169:8–18
33. Tarpan MA, De Cooman H, Sagstuen E et al (2011) Identification of primary free radicals in trehalose dihydrate single crystals X-irradiated at 10 K. Phys Chem Chem Phys 13:11294–11302. doi:10.1039/c0cp02616f
34. Box HC (1977) Radiation effects: ESR and ENDOR analysis. Academic Press, New York
35. Tarpan MA, Pauwels E, Vrielinck H et al (2010) Electron magnetic resonance and density functional theory study of room temperature X-irradiated β-D-fructose single crystals. J Phys Chem A 114:12417–12426. doi:10.1021/jp107777v
36. Barone V, Adamo C, Grand A et al (1995) Structure and ESR features of glycine radical. J Am Chem Soc 117:12618–12624. doi:10.1021/ja00155a026

37. Declerck R, Pauwels E, Speybroeck V Van, Waroquier M (2008) Molecular environment and temperature dependence of hyperfine interactions in sugar crystal radicals from first principles. J Phys Chem B 112:1508–1514. doi:10.1021/jp076571w
38. Kay CWM, Schleicher E, Hitomi K et al (2005) Determination of the g-matrix orientation in flavin radicals by high-riel/high-frequency electronnuclear double resonance. Magn Reson Chem 43:S96–S102. doi:10.1002/mrc.1667
39. Kumar A, Pottiboyina V, Sevilla MD (2012) One-electron oxidation of neutral sugar radicals of 2 `-deoxyguanosine and 2 `-deoxythymidine: a density functional theory (DFT) Study. J Phys Chem B 116:9409–9416. doi:10.1021/jp3059068
40. Pauwels E, Asher J, Kaupp M, Waroquier M (2011) Cluster or periodic, static or dynamic-the challenge of calculating the g tensor of the solid-state glycine radical. Phys Chem Chem Phys 13:18638. doi:10.1039/c1cp21452g
41. Pauwels E, Declerck R, Verstraelen T et al (2010) Influence of protein environment on the electron paramagnetic resonance properties of flavoprotein radicals: a QM/MM study. J Phys Chem B 114:16655–16665. doi:10.1021/jp109763t
42. Pauwels E, Verstraelen T, De Cooman H et al (2008) Temperature study of a glycine radical in the solid state adopting a DFT periodic approach: vibrational analysis and comparison with EPR experiments. J Phys Chem B 112:7618–7630. doi:10.1021/jp711997y
43. Petrenko TL (2002) Transformation and structure of cation radicals in L-alpha-alanine. J Phys Chem A 106:149–156. doi:10.1021/jp0106395
44. Tachikawa H, Takada T (2013) Ionization dynamics of the water trimer: a direct ab initio MD study. Chem Phys 415:76–83. doi:10.1016/j.chemphys.2012.12.027
45. Tachikawa H, Fukuzumi T (2011) Ionization dynamics of aminopyridine dimer: a direct ab initio molecular dynamics (MD) study. Phys Chem Chem Phys 13:5881–5887. doi:10.1039/c0cp01542c
46. Aalbergsjø SG, Pauwels E, Van Yperen-De Deyne A, Van Speybroeck V, Sagstuen E (2014) Automated generation of radical species in crystalline carbohydrates using ab initio MD simulations. Phys Chem Chem Phys 16: 17196-17205. doi: 10.1039/c4cp02179g
47. Pauwels E, Lahorte P, Vanhaelewyn G et al (2002) Tentative structures for the radiation-induced radicals in crystalline beta-D-fructose using density functional theory. J Phys Chem A 106:12340–12348. doi:10.1021/jp0264174
48. Frisch MJ, Trucks GW, Schlegel HB et al (2009) Gaussian 09, Revision A.02. Gaussian Inc Wallingford CT 34:Wallingford CT. doi:10.1159/000348293
49. Asher JR, Kaupp M (2008) Car-Parrinello molecular dynamics simulations and EPR property calculations on aqueous ubisemiquinone radical anion. Theor Chem Acc 119:477–487. doi:10.1007/s00214-007-0408-1
50. CPMD. http://www.cpmd.org, 1990–2008, Copyright IBM Corp 1997-2001, Copyright MPI für Festkörperforschung Stuttgart
51. Becke AD (1996) Density-functional thermochemistry.4. A new dynamical correlation functional and implications for exact-exchange mixing. J Chem Phys 104:1040–1046. doi:10.1063/1.470829
52. Bussi G, Donadio D, Parrinello M (2007) Canonical sampling through velocity rescaling. J Chem Phys 126:014101. doi:10.1063/1.2408420
53. Hoover WG (1985) Canonical dynamics: equilibrium phase-space distributions. Phys Rev A 31:1695–1697. doi:10.1103/PhysRevA.31.1695
54. Nosé S (1984) A unified formulation of the constant temperature molecular dynamics methods. J Chem Phys 81:511. doi:10.1063/1.447334
55. Sagstuen E, Sanderud A, Hole EO (2004) The solid-state radiation chemistry of simple amino acids, revisited. Radiat Res 162:112–119. doi:10.1667/rr3215
56. Debije MG, Bernhard WA (2001) Electron paramagnetic resonance evidence for a C3′ sugar radical in crystalline d(CTCTCGAGAG) X-irradiated at 4 K. Radiat Res 155:687–692. doi:10.1667/0033-7587(2001)155[0687:EPREFA]2.0.CO;2
57. Koch W, Holthausen MC (2001) A chemist's guide to density functional theory. 3:294. doi:10.1002/3527600043

58. Peng CY, Ayala PY, Schlegel HB, Frisch MJ (1996) Using redundant internal coordinates to optimize equilibrium geometries and transition states. J Comput Chem 17:49–56. doi:10.1002/(SICI)1096-987X(19960115)17:1%3C49::AID-JCC5%3E3.0.CO;2–0
59. Adhikary A, Kumar A, Heizer AN et al (2013) Hydroxyl ion addition to one-electron oxidized thymine: unimolecular interconversion of C5 to C6 OH-adducts. J Am Chem Soc 135:3121–3135. doi:10.1021/ja310650n
60. Adhikary A, Kumar A, Palmer BJ et al (2013) Formation of S-Cl phosphorothioate adduct radicals in dsDNA S-oligomers: hole transfer to guanine vs disulfide anion radical formation. J Am Chem Soc 135:12827–12838
61. Elber R, Karplus M (1987) A method for determining reaction paths in large molecules: application to myoglobin. Chem Phys Lett 139:375–380. doi:10.1016/0009-2614(87)80576-6
62. Henkelman G, Jonsson H (2000) Improved tangent estimate in the nudged elastic band method for finding minimum energy paths and saddle points. J Chem Phys 113:9978–9985. doi:10.1063/1.1323224
63. Henkelman G, Uberuaga BP, Jonsson H (2000) A climbing image nudged elastic band method for finding saddle points and minimum energy paths. J Chem Phys 113:9901–9904. doi:10.1063/1.1329672
64. Pauwels E, De Cooman H, Waroquier M et al (2014) Solved? The reductive radiation chemistry of alanine. Phys Chem Chem Phys 16:2475–2482. doi:10.1039/c3cp54441a
65. Li X, Sanche L, Sevilla MD (2006) Base release in nucleosides induced by low-energy electrons: a DFT study. Radiat Res 165:721–729. doi:10.1667/RR3568.1
66. Sagstuen E, Close DM, Vågane R et al (2006) Electron transfer in amino acid.nucleic acid base complexes: EPR, ENDOR, and DFT study of X-irradiated N-formylglycine.cytosine complex crystals. J Phys Chem A 110:8653–8662. doi:10.1021/jp0610822
67. De Cooman H (2009) A combined EMR and DFT study of radiation-induced defects in sucrose and glucose 1-phosphate. PhD Thesis, Ghent University.
68. Von Sonntag C, Schuchmann H-P (2001) Carbohydrates. In: Jonah CD, Rao BSM (eds) Radiation chemistry present status future trends. Elsevier, Amsterdam, pp 481–512
69. Von Sonntag C (1987) The chemical basis of radiation biology. 515
70. Sagstuen E, Hole EO (2009) Radiation produced radicals. In: Brustolon M, Giamello E (eds) Electron paramagnetic resonance a practitioner's toolkit. Hoboken New Jersey: John Wiley & Sons, pp 325–382
71. Pulay P (1980) Convergence acceleration of iterative sequences—the case of SCF iteration. Chem Phys Lett 73:393–398. doi:10.1016/0009-2614(80)80396-4